Department of Construction Sciences
Division of Solid Mechanics

ISRN LUTFD2/TFHF-26/5276-SE

Analysis of the impact of residual stress on instability and collapse of submarine pressure hulls

Master's Dissertation by
Greta Garme & Jesper Olanders

Supervisors:
Anders Ericsson, PhD, Saab Naval
Martin Fisk, Senior Lecturer, Division of Solid Mechanics, LTH

Examiner:
Ralf Denzer, Senior Lecturer, Division of Solid Mechanics, LTH

For information, address:
Division of Solid Mechanics, Lund University, Box 118, SE-221 00 Lund, Sweden
Webpage: www.solid.lth.se

Preface

During the spring semester we have carried out our master's thesis at the Structural Analysis department at Saab's office in Lund. We have felt very welcomed by everyone in the team and have truly enjoyed our months here.

First and foremost, we would like to thank Anders Ericsson at Saab, for his great commitment, patience, and for always being an excellent sounding board. No question has ever felt too small or too simple to ask Anders and the many hours we have spent discussing residual stresses have been both educational and fun despite the complex subject. Furthermore, we would like to thank Martin Fisk at LTH for his expertise in the subject and support in writing the report.

We would also like to thank our consultant colleagues, Torulf, Per and Oskar for their help whenever HyperMesh and Abaqus gave us headaches. In addition to helping with software, they have been a great support and showed much care throughout the project.

Finally, we would like to thank our fellow master's thesis student friends from LTH for brightening our lunches under the cork oak throughout the semester. A well-needed break from studying stiffened cylinders for hours.

Greta & Jesper,

Lund, June 2026

Abstract

Residual stresses and geometric imperfections are unavoidable consequences when manufacturing a submarine pressure hull. These effects can reduce collapse pressure by promoting earlier yielding, particularly in regions subjected to compressive stresses.

In this work, nonlinear finite element analyses were performed on ring stiffened segments of a pressure hull using Abaqus to investigate how residual stresses and geometric imperfections influence the collapse behavior. Residual stresses from welding and cold bending were implemented as initial stress fields using distributions from British Standard 7910:2019 and analytical cold bending formulations applied to pre-defined manufacturing-affected element sets. To investigate the effect of solely geometric imperfections, displacement fields obtained from relaxation of the residual stress state were imported as initial imperfections in separate analyses. Both the individual effect of residual stresses and the combined effect were studied.

The results show that cold bending, plating-web fillet welds and girth welds have the most significant influence on collapse pressure. Both residual stresses and geometric imperfections reduce the collapse pressure, but residual stresses have a stronger influence. Relative to the ideal, stress-free analysis of nominal geometry, residual stresses in combination with geometric imperfections reduce the collapse pressure by 10.5 – 14.6%, whereas the corresponding effect of solely geometric imperfections is 5.0 – 6.8% for the tested cases. This thesis improves the understanding of how different manufacturing-induced residual stress sources influence collapse behavior and shows that the governing mechanism is closely linked to the introduction of compressive stresses in vulnerable regions.

Table of contents

1 Introduction

Submarines operate under external hydrostatic pressure, which increases linearly with diving depth. This imposes strict requirements on the structural integrity of the pressure hull, the cylindrical shell structure responsible for resisting the external pressure load. For military submarines, these requirements are particularly demanding due to operational requirements. Structural failure of the pressure hull, whether by buckling or plastic collapse, would have catastrophic consequences. Therefore, accurate prediction of its load-carrying capacity and understanding of all loads and stresses are essential for safe and efficient design.

During manufacturing, processes such as cold bending and welding are central for manufacturing cylindrical shell sections. However, these processes also introduce residual stresses into the material. Cold bending generates stresses due to plastic deformation, while welding induces residual stresses through localized heating and cooling. In addition, welding may introduce geometric imperfections, causing the pressure hull to deviate from an ideal cylindrical shape. These deviations are unavoidable, as manufacturing processes cannot produce perfectly ideal geometries.

Both residual stresses and geometric imperfections have an effect on structural performance, reducing the collapse pressure of the pressure hull. The extent of this effect depends on several factors, including the amplitude and wavelength of the imperfections, as well as the level of residual stresses [1].

The effect of both residual stresses and geometric imperfections has been previously studied in the literature. Robertsson [1] investigated residual stresses arising from cold bending and welding in submarine hulls, while Faulkner [2] examined the detrimental effect of fabrication-induced residual stresses and imperfections on the compressive strength of stiffened shells and panels. Franquetto and Neto [3] later quantified residual stress distributions experimentally on a submarine pressure hull, approximating the through-thickness distributions by polynomial functions and incorporated these into nonlinear finite element analyses to evaluate their effect on collapse pressure. Similarly, Ficquet [4] measured residual stresses on a Rubis-class pressure hull section using deep hole drilling, providing experimental data to support fatigue, fracture, and numerical modeling. Both Kendrick [5] and Franquetto [3] state that the influence of residual stress becomes less pronounced when geometric imperfections are present. For example, residual stress may reduce the collapse pressure by approximately 13% for an out-of-circularity of 0.25%, but only by about 4% for an out-of-circularity of 1% [5].

Although the influence of geometric imperfections is well investigated, the influence of residual stresses has not been studied as extensively. This is likely because of the complexity in obtaining measurements of the residual stress of a submarine pressure hull. Residual stresses are internal and self-equilibrating and can therefore not be measured as directly and straight-forward as geometric imperfections.

The aim of this thesis is to investigate how residual stresses and the corresponding geometric imperfections influence the collapse behavior of a ring stiffened submarine pressure hull subjected to external pressure. The specific objectives are:

- to study the influence of residual stress arising from cold forming and welding on the collapse pressure,
- to study the combined effect of residual stresses from several welding types on structural capacity,
- to compare the reduction in collapse pressure caused by residual stresses with that caused by the corresponding geometric imperfections,
- to analyze the mechanism by which residual stresses influence collapse behavior.

The scope of the thesis is limited to only study the local effects within a region of a few stiffener bays, rather than the global behavior of the entire pressure hull.

2 Stability and strength under external pressure

A submarine typically consists of two main structural components: the casing and the pressure hull. The casing, also referred to as the hydrodynamic hull, primarily provides hydrodynamic streamlining and houses external equipment [6]. The space between the casing and the pressure hull is generally waterfilled, resulting in the casing being exposed to nearly equal pressure on both sides and does therefore not carry the hydrostatic pressure load [6]. The pressure hull, on the other hand, is the structure designed to withstand the external pressure and maintains the structural integrity of the submarine [6]. Consequently, the design and configuration of the pressure hull largely determine the operational limits and performance of the vessel.

A spherical shell provides the most efficient geometry for resisting external pressure; however, these pressure vessels are generally impractical for submarines because they are difficult to manufacture, inefficient in terms of internal space utilization and unsuitable for docking and accommodating crew and equipment [6]. For these reasons, a cylindrical pressure hull is mostly used, as they are easier to manufacture with sufficient precision while still providing adequate resistance to external pressure [6].

The pressure hull is usually designed as a tear-drop shaped structure consisting of cylindrical and conical shells, terminated by domes [7]. A cylindrical pressure hull is typically formed from cold bent metal plates, which is preferred because curved plates can resist pressure loads primarily through membrane stress rather than bending stress, resulting in a more efficient load-carrying behavior [6]. To improve structural stability, the pressure hull is reinforced with ring stiffeners and bulkheads. The ring stiffeners consist of a web and a flange, where the web is the plate oriented normal to the plating and the middle of the flange is attached to the free edge of the web, making a T-cross section. These ring stiffeners increase the resistance of the shell to elastic instability and help postpone buckling before yielding and eventual failure [7] and can be placed both internally and externally [6]. Bulkheads are watertight structural elements that divide the pressure hull into compartments, allowing individual sections of the submarine to be isolated in emergency situations [6]. Although bulkheads can be modeled as rigid boundaries for simplicity, the present work considers only a limited number of stiffeners and focuses on local behavior; bulkheads are therefore not included in the model. An illustration of a pressure hull, including ring stiffeners and bulkheads is given in Figure 2.1.

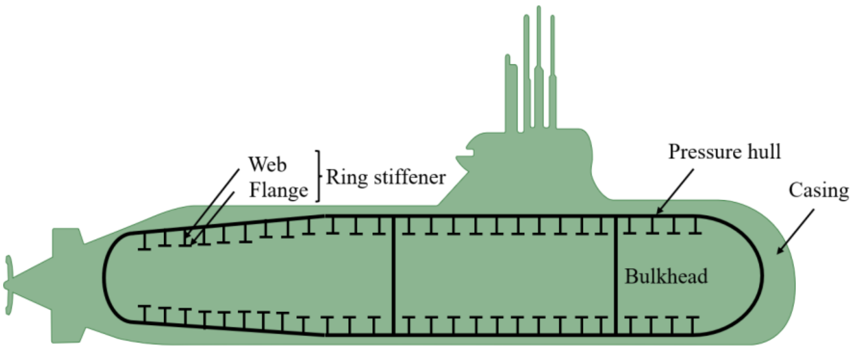

Figure 2.1: Casing (green) and pressure hull (black) with ring stiffeners consisting of webs and flanges and bulkheads.

The pressure hull is usually fabricated from high-strength steels selected based on a balance between mechanical properties and manufacturability. The shell plating and stiffeners are primarily assembled by welding, which introduces residual stresses and geometric imperfections in the structure. These manufacturing effects are inevitable and may significantly reduce the buckling pressure [7].

When subjected to external pressure, ring stiffened cylindrical shells may buckle in several modes, including interstiffener buckling, stiffener tripping and overall shell buckling [6]. These failure mechanisms, together with the influence of material yielding and manufacturing-induced imperfections, are central to the structural design of submarine pressure hulls. The following subsections present the theoretical background for elastic instability and plastic collapse.

2.1 Elastic instability

For a cylindrical pressure hull, the external hydrostatic loading gives rise to both circumferential and axial compressive stresses. The radial pressure acts normal to the shell surface at all points, while the axial load arises from the pressure acting on the end bulkheads and is transmitted through the cylindrical plating in the axial direction. These compressive stresses contribute to the instability behavior of the shell structure.

Elastic buckling refers to instability occurring while the material remains in the elastic range. This means that the structure has not reached its yield limit and would, in principle, return to its original configuration upon unloading. To introduce elastic instability, Euler's column theory may be recalled, where a structure subjected to compressive loading loses stability when a critical load is reached. However, the buckling behavior of cylindrical shells is more complex, where instability may occur through different deformation patterns involving both axial and circumferential displacements [8].

For cylindrical shells subjected to compressive loading, the stability response is strongly dependent on parameters such as geometry, boundary conditions and geometric imperfections [8]. Compared to a simple column buckling, thin-walled cylinders are particularly sensitive to small deviations from the ideal geometry. This makes manufacturing-induced imperfections important to consider when evaluating the collapse behavior of pressure hull structures.

Stability analysis examines how a system responds to perturbations, which for a submarine could be external loading, geometric imperfections or dynamic perturbations such as underwater explosions. The central question in stability analysis is whether the system remains close to its original state after a disturbance or whether the deviation grows, leading to instability [9].

An equilibrium point represents a state where the structure remains in balance under a given load. As the applied load increases, these points form an equilibrium path along which the stability of the structure may change [9]. A bifurcation point occurs when multiple equilibrium paths intersect, allowing the system to transition to an alternative configuration, possibly associated with buckling [9, 10].

For an ideal cylindrical shell, the structure first follows a stable pre-buckling path. When the critical buckling load is reached, the shell may experience a sudden transition to a different equilibrium state, referred to as bifurcation buckling [8]. Beyond this point, the structure follows a post-buckling path, where additional deformation occurs. This general instability is illustrated in Figure 2.2 for a cylindrical shell subjected to axial compressive loading.

In practical applications, geometric imperfections and material nonlinearities modify this idealized behavior. Instead of a sudden bifurcation, deformation develops gradually with increasing load. Collapse is therefore typically governed by nonlinear elastic-plastic effects, where increasing geometric imperfections generally reduce the buckling load [1].

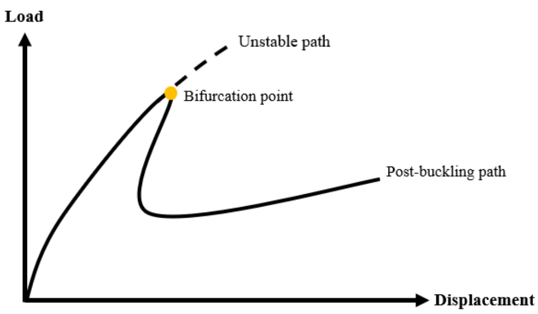

Figure 2.2: Equilibrium path for a cylindrical shell subjected to axial compressive loading, illustrating the transition from the initial equilibrium path to a post-buckling behavior through bifurcation buckling.

For pressure hull design, accurate prediction of the critical external pressure is essential. A ring stiffened cylindrical shell subjected to external pressure may buckle in several distinct deformation patterns, commonly referred to as buckling modes. Although an infinite number of theoretical modes exist, practical design typically considers three primary modes: interstiffener buckling, overall buckling and stiffener tripping [5].

Interstiffener buckling occurs when the shell plating buckles locally between adjacent stiffeners, forming lobes in the circumferential direction. Overall buckling involves deformation of the entire shell structure, where both the shell and the stiffeners deform simultaneously. Ultimately, stiffener tripping is a form of a local stiffener instability which occurs when the stiffener itself buckles. These modes are all illustrated in Figure 2.3.

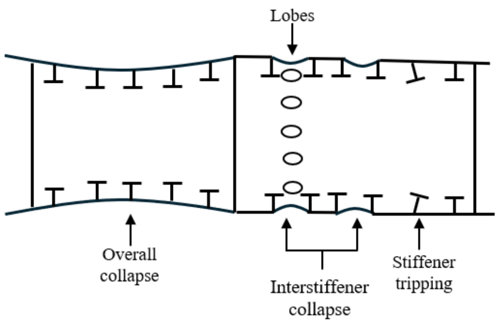

Figure 2.3: Illustration of common buckling modes, including overall collapse, interstiffener collapse and stiffener tripping.

The selection of design variables such as material properties, shell thickness, pressure hull radius and stiffener spacing strongly influences the structural integrity against external pressure [5]. Structures with heavy and stiff stiffeners tend to fail by interstiffener buckling while, in contrast, lighter stiffeners increase the susceptibility to overall buckling [1]. If the stiffeners are slender, especially with thin webs, stiffener tripping may become the dominant failure mode [1].

When dimensioning a pressure hull, design may be governed by either elastic instability or plastic collapse. Due to the sensitivity and unpredictability of elastic buckling, safety factors are applied such that the operational pressure remains well below the predicted plastic collapse pressure [1].

2.2 Plastic collapse

Buckling can be viewed as a stability failure, whereas plastic collapse is a strength failure associated with irreversible deformation. This section introduces different material models, followed by a discussion of yielding and plastic collapse.

The behavior of an elasto-plastic material is initially linear elastic with Young's modulus E, until the initial yield stress σ_{y0} is reached. Beyond this point, yielding occurs and plastic strains start to develop in the material. If an elasto-plastic strain hardening material is unloaded at this point, the strain will decrease, following a linear path with slope E, shown in Figure 2.4 a). In addition to this material model, several models exist that represent plastic behavior, where one simplified response is elastic-perfectly plastic. This model is characterized by a linear elastic region up to the initial yield stress σ_{y0}, followed by perfectly plastic behavior at constant stress, illustrated in Figure 2.4 b).

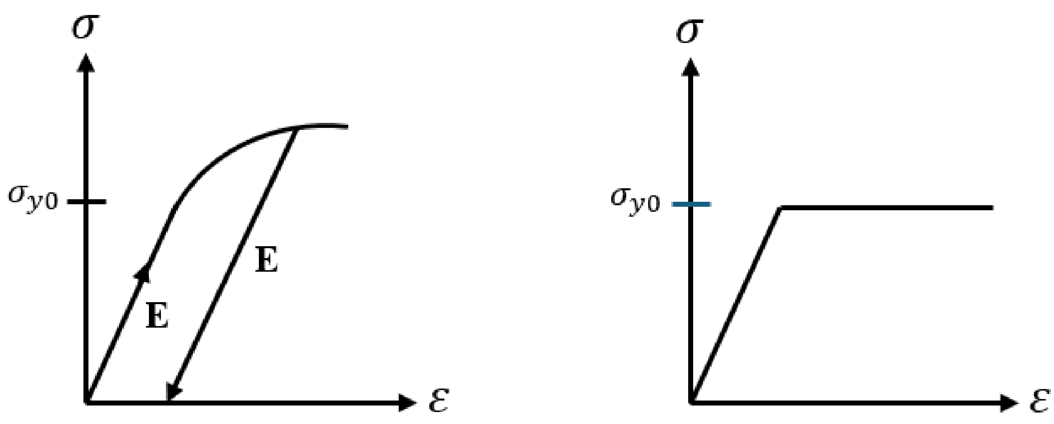

a) b)

Figure 2.4. Material responses for a) an elasto-plastic material exhibiting strain hardening and b) an elastic-perfectly plastic material without strain hardening.

Although real materials typically exhibit strain hardening after yielding, this is neglected in the ideal plastic model. Consequently, the current yield stress σ_y coincides with the initial yield stress σ_{y0} and the yield surface remains fixed in stress space without changing size or shape [10]. Due to this simplification, the elastic-perfectly plastic model provides a conservative estimate of structural capacity, as it neglects the additional strength that arises from strain hardening.

When the stress in the structure reaches the yield stress, local plastic deformation begins. Once plastic deformation has occurred, the structure cannot return to its original configuration and its ability to carry load is reduced. As parts of the structure yield, the stress is redistributed to the remaining elastic regions. Since the extent of elastic regions decreases as yielding spreads, higher stresses develop in these regions, which in turn accelerates further yielding.

The bending moment at which yielding first occurs in a cross-section is called the yield moment M_y. With increasing load, plasticity spreads across the section until it is fully yielded, corresponding to the plastic moment M_p [11]. At this point, a plastic hinge forms, which has no additional moment capacity but allows rotation. The formation of plastic hinges enables redistribution of internal forces within the structure. As the load increases and more hinges develop, additional sections reach their yield limit which reduces the structure's ability to sustain further load without undergoing large deformations. When the structure is no longer able to carry any additional load, the structure has reached plastic collapse.

3 Residual stresses arising from pressure hull manufacturing

Residual stresses and geometric imperfections are introduced during the manufacturing process of the pressure hull and may both reduce the structural capacity under external pressure. Cold bending and welding are the manufacturing methods that will be considered in this thesis, both introducing different residual stresses in the structure caused by different mechanisms. Geometric imperfections are introduced to the hull through both fabrication and assembly in the form of tolerances and from the residual stresses which will distort the hull from the ideal cylinder shape.

Residual stresses can be classified according to the mechanism by which they arise, the length scale over which they equilibrate, or their effect on structure behavior. Withers [12] classifies residual stresses into three characteristic length scales. Type I residual stresses, also referred to as macro stresses, act at the continuum level and equilibrate over a length scale comparable to the dimensions of the component. These stresses arise, for example, from bending and steep temperature gradients. Type II stresses are intergranular stresses which arise on the microstructural scale due to heterogeneous deformation between neighboring grains. Type III stress exists at an even finer scale, arising from lattice defects at the atomic scale. In this thesis, the focus lies on type I stresses since the manufacturing methods considered primarily introduce stresses at the structural scale [12].

At a given location in the shell, residual stresses are represented by through-thickness profiles of the in-plane stress components. In shell theory, a cylindrical coordinate system is used, defined by the radial coordinate *r*, the angular coordinate θ and the longitudinal coordinate x. In this system, the in-plane stress components are the axial stress, acting parallel to the cylinder axis, and the circumferential stress component acting in the θ direction, also referred to as hoop stress [3]. The radial stress component is typically small compared to the in-plane stresses and therefore, shells are commonly analyzed using a plane stress assumption where the out-of-plane (radial) stress component is neglected [1].

At a given location, the axial and circumferential residual stress profiles can be decomposed into three components: membrane stress (σ_m), bending stress (σ_b) and self-equilibrating stress (σ_{sb}). For this decomposition, the through-thickness coordinate z is measured from the shell inner surface, ranging from *0* to h, where h is the material thickness. The residual stress is thus decomposed according to

$$\sigma = \sigma_m + \sigma_b(z) + \sigma_{sb}(\mathrm{z}) \tag{3.1}$$

The membrane stress is the through-thickness average and therefore contributes to a resultant force but no bending moment,

$$\sigma_m = \frac{1}{h}\int_0^h \sigma(z)\, dz \tag{3.2}$$

The bending stress varies linearly through the thickness and contributes to the bending moment, while the through-thickness resultant is zero,

$$\int_0^h \sigma_b(z)\, dz = 0$$

$$M = \int_0^h \sigma_b(z)\,(z - h/2)\, dz \tag{3.3}$$

Since the through-thickness coordinate z is measured from the inner surface, the bending moment is evaluated with respect to the mid-plane using the lever arm $(z-h/2)$. Remaining is the self-equilibrating stress component which represents the variation of stress after the membrane and bending components have been removed and exists to fit through-thickness curves to experimentally measured stress profiles. This component contributes neither to a net force nor to a bending moment [13].

$$\int_0^h \sigma_{sb}(z)\, dz = 0$$

$$M = \int_0^h \sigma_{sb}(z)\,(z - h/2)\, dz = 0 \tag{3.4}$$

Together, these three components reconstruct the actual through-thickness stress state according to Equation (3.1), while individually they provide a convenient way of distinguishing between different mechanical effects. The local residual stress distribution may contain membrane forces and bending moments even though the residual stresses are globally in equilibrium [2, 3]. These local resultants can cause contraction, expansion, or bending of the structure and thereby contribute to geometric imperfections.

When the hull is subjected to external pressure, compressive stresses are introduced in both the longitudinal and circumferential directions. Within regions with an initial compressive residual stress, the combination of residual and compressive stress due to external pressure causes the effective stress to approach yield stress earlier than an ideal, stress-free structure. Thus, yielding may occur at a lower pressure than predicted for an ideal structure would and thus lowering the collapse pressure [3].

3.1 Cold bending of plates

In hull manufacturing, flat steel plates are bent into circular sectors by cold bending. In this process a set of rollers gradually introduces and increases curvature on the material until the desired radius is achieved. When bending, the outer surface is subjected to tensile strains and the inside surface compressive strains, shown in Figure 3.1 a). With a sufficiently small radius, the material near the surfaces undergoes plastic deformation while the interior of the plate may remain elastic, shown in Figure 3.1 b). When the external forces from the rollers are removed, the elastic portion of the material partially recovers causing the spring back phenomenon where the radius increases. This results in a characteristic zig-zag or Z-shaped residual stress profile, shown in Figure 3.1 c), that is in self-equilibrium [1, 4].

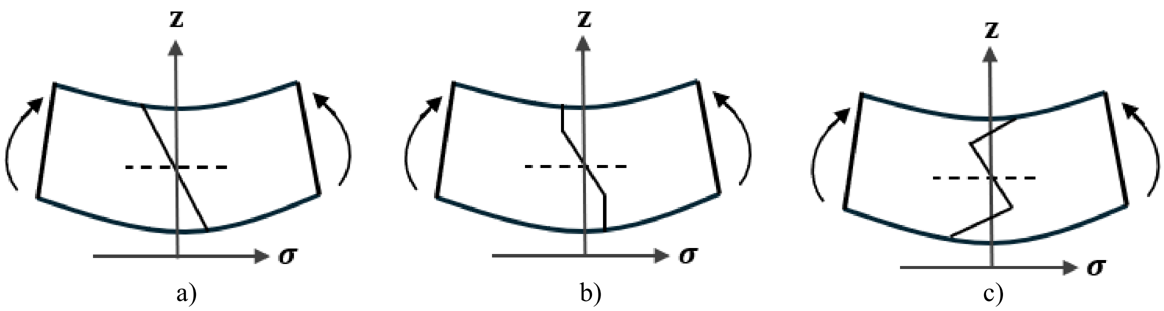

Figure 3.1 Bending residual stress with an elastic-perfectly plastic assumption for a) bent within elastic response, b) bent to plastically deform at surfaces, and c) resulting residual stress profile after spring back.

Analytical expressions for this cold bending residual stress distribution can be derived from elastic-plastic bending theory. In the formulation presented by Robertson [1], an elastic-perfectly plastic plate is bent to the initial radius and allowed to spring back to the final radius. The variables for the derivation are defined as: R_0 = initial radius before springback, $R =$ final radius after spring back, $h =$ plate thickness, $\rho =$ through thickness coordinate from the plate mid-plane given by $\rho = z - h/2$ and ranges between $\pm h/2$ (shown in Figure 3.2), $\sigma_y =$ yield stress and $E =$ Young's modulus. For a plate with known geometry and material properties, the dimensionless parameter F is defined as

$$F = \frac{Eh}{\sigma_y R} \tag{3.5}$$

The initial radius R_0 required to obtain the final radius R is determined from the condition of zero resultant moment in the final state, which gives

$$M = 0 = 2\int_0^{\sigma_y R_0/E} E\rho^2/R\, d\rho + 2\int_{\sigma_y R_0/E}^{h/2} \sigma_y \rho - E\rho^2(1/R_0 - 1/R) d\rho \tag{3.6}$$

From the zero-moment condition, the following relation between the initial radius R_0, final radius R and the parameter Q becomes

$$R_0 = R(4 - 3Q^2 + Q^3)/Q^3 \tag{3.7}$$

where $Q = Eh/(\sigma_y R_0)$. Using this, the dimensionless parameter F in Equation (3.5) can be expressed in terms of Q as

$$F = Q\frac{R_0}{R} \tag{3.8}$$

Substituting the expression for $\frac{R_0}{R}$ from Equation (3.7) into Equation (3.8) gives

$$F = \frac{Eh}{\sigma_y R} = \frac{R_0 Q}{R} = \frac{4 - 3Q^2 + Q^3}{Q^2} \tag{3.9}$$

Equation (3.9) is solved for Q. For the three solutions, the physically correct solution must be real and $R_0 < R$, since the springback increases the final radius after unloading. With Q established, R_0 follows from Equation (3.7), and the residual stress distribution for linear strain and elastic springback is obtained as

$$\sigma_\theta = \begin{cases} \dfrac{E\rho}{R}, & \rho < \dfrac{\sigma_y R_0}{E} \\ \sigma_y - E\rho(1/R_0 - 1/R), & \rho > \dfrac{\sigma_y R_0}{E} \end{cases} \tag{3.10}$$

This formulation is used in the present work to generate the through-thickness residual stress profile associated with cold bending, see Figure 3.2. The geometry is defined by the normalized stress levels σ_1/σ_y, σ_2/σ_y, and the normalized transition depth ζ_t/h, defined as

$$\sigma_1/\sigma_y = R_0/R = (4 - 3Q^2 + Q^3)/Q^3 \tag{3.11}$$

$$\sigma_2/\sigma_y = (4 - Q^2)/2Q^2 \tag{3.12}$$

$$\zeta_t/h = 2/Q \tag{3.13}$$

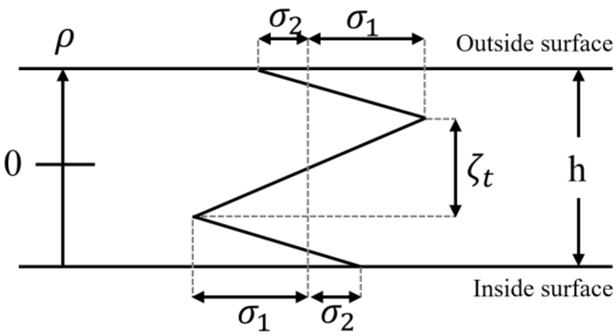

Figure 3.2 Self-balancing elastic-perfectly plastic through-thickness residual stress distribution after cold bending, where ρ is the through thickness coordinate from the plate mid-plane illustrated to the left and h is the plate thickness.

Franquetto and Neto [3] report experimental measurements from an S80-class submarine (submarines used in the Spanish navy), obtained from the deep hole drilling (DHD) method, combined with X-ray measurements of residual stress at the internal and external surfaces. Two through-thickness stress profiles measured far from weld joints are presented, where the residual stresses are assumed to mainly be influenced by the cold bending process. One profile for the cold bent plating and one for the cold bent flange are included, both approximately self-equilibrating through the thickness [3]. Both show the characteristic zig-zag distribution, however, compared to the analytical profile, the measured profiles are smoother. This reflects the influence of strain hardening that the material realistically undergoes, as well as manufacturing conditions that differ from the idealized assumptions given by Equations (3.5) - (3.13).

3.2 Residual stresses from welding

Welding joins components by melting a small portion of metal, which solidifies into a joint piece. Typically, fusion welding is conducted by moving a heat source along the weld line, which creates a time-dependent temperature field in the surrounding material. The temperature is highest under the heat source and gradually decreases with different gradients along the weld line, away from the heat source and into the surrounding material outside the weld line. This results in a non-uniform heat distribution. Material heated above the melting temperature forms the weld metal, and material heated above the transformation temperature but below the melting temperature forms the heat-affected zone (HAZ). The joining process is divided into the heating, melting and solidification process resulting in residual stresses [14].

Different weld types exist, varying in configuration of joint components and joint preparation which results in different characteristics. For pressure hulls, joints considered in this work are butt joints, joining aligned plates and T-joints joining components perpendicular to each other. The weld types assumed are double V groove (DV) for butt joints and fillet weld for the T-joints as illustrated in Figure 3.3. The surface of the grooves has the function of increasing the area that is melted, creating a larger weld penetration and results in a stronger bond between the joined components [14].

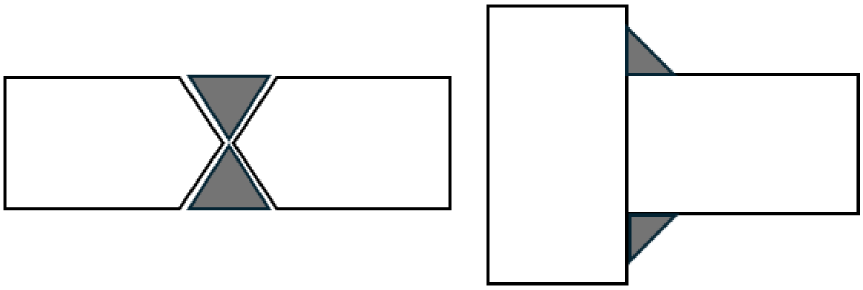

a) Double V groove (DV) butt welds b) Fillet weld

Figure 3.3 Schematic of the considered weld types, white = the components, grey = added material from welding.

In welding, the non-uniformity and time dependence of the temperature distribution and the temperature dependence of thermal expansion result in non-uniform thermal expansion and contraction, where the cooler material acts as mechanical restraint [14]. During heating, the material near the weld expands which is restrained by the surrounding cooler material, generating compressive stresses. During cooling, the weld and HAZ contract, which, again, is restrained by the surrounding material, leading to tensile residual stresses, often approaching yield stress in and near the weld. The difference in expansion and contraction results in different magnitudes of elastic and/or plastic strains, meaning that when the structure cools down to ambient temperature, permanent strains remain locked in the material, forming residual stresses [14].

The residual stress field is characterized by three mechanisms, longitudinal shrinkage (along the weld) creating tensile stresses parallel to the weld, transverse shrinkage (perpendicular to the weld), and through-thickness gradients, leading to bending-type stress distributions [14]. Residual stresses from welding are difficult to measure and strongly depend on the welding process and geometry [3]. Therefore, standardized residual stress profiles can be used for assessments. British standard 7910:2019 Annex Q (henceforth called BS 7910) provides through-thickness residual stress distributions for typical weld geometries, obtained from arc welds without post-weld heat treatment (annealing) for pipeline structures with thick shells, comparable to the pressure hull of submarines [15]. The profiles in BS 7910 represent upper-bound fit of the experimental data, providing conservative stress profiles. BS 7910 decomposes both longitudinal and transverse residual stress through-thickness profiles into three components: membrane stress that is constant through-thickness, bending stress that varies linearly through the thickness, and a self-balancing stress which is a fitted fourth-order polynomial. The magnitude and distribution of each component vary for the considered weld geometry [15]. In BS 7910, the profiles are expressed as functions of the normalized through-thickness depth z/h, ranging from 0 at the inner surface to 1 at the outer surface.

In addition to the through-thickness distribution, the weld must also be assigned a characteristic width defining the region over which the residual stress state is significantly affected. Dong et al. [13] present a detailed shell-theory based formulation in which the residual stress field is described as a function of distance from the weld toe. The distribution is influenced by the characteristic heat input and thereby several underlying weld parameters [13]. Other approaches use simpler thickness-based estimates.

3.2.1 Weld types in the pressure hull

In the weld literature, directions are described as longitudinal and transverse relative to the weld line. In the present work, these directions are interpreted as the axial and circumferential directions of the hull, depending on the orientation of the weld. As previously discussed, welding-induced deformation in welded joints is commonly described by longitudinal and transverse shrinkage, as well as rotational and angular distortion, where the latter results in bending [14]. Welding is extensively used in the fabrication of pressure hulls. In this work, four principal weld configurations are considered: plating-web welds, web-flange welds, seam welds (axial direction) and girth welds (circumferential direction). Their locations within the pressure welds are illustrated in Figure 3.4.

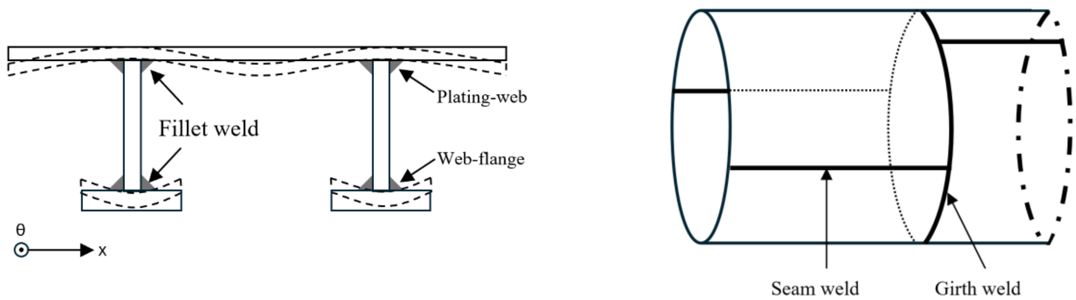

a) Fillet welds and the corresponding deformation

b) Seam and girth welds

Figure 3.4 Principal weld configurations in the pressure hull: a) T-fillet welds and b) seam and girth welds.

Between the plating and web, as well as between the web and flange, fillet welds are assumed. For these welds, the weld line follows the circumferential direction, so that the weld longitudinal direction follows the hull circumferential direction and the transverse direction follows the hull axial direction. Fillet welds introduce both longitudinal and transverse shrinkage, where longitudinal shrinkage generates residual tensile stresses along the weld direction, corresponding to the circumferential direction. Transverse shrinkage, on the other hand, includes bending moments due to asymmetric contraction through the thickness [1]. For plating-web welds, this results in inward radial deformation of the plating between the stiffeners, see Figure 3.4 a). In contrast, web-flange welds exhibit similar mechanisms but typically induce deformation in the opposite (outward) radial direction as shown in Figure 3.4 a) [1]. Hoop and axial residual stress profiles are presented both in BS 7910 [15] and by Franquetto and Neto [3] as experimental measurements.

For seam and girth welds, DV butt joints are assumed in the present work, see Figure 3.3 b). The seam welds join the bent plates to close the hull circumference and are used on both the plating and the flange, whereas girth welds connect cylindrical sections. The weld orientation differs between the two cases: the longitudinal weld direction is aligned with the axial direction for seam welds and with the circumferential direction for girth welds. Since welding-induced contraction is unavoidable, the groove geometry can be altered to control the resulting distortion. Longitudinal shrinkage primarily leads to residual stresses in the weld direction, while transverse shrinkage contributes to bending deformation. Consequently, seam welds tend to generate axial residual stresses and circumferential (hoop) bending, whereas girth welds produce circumferential residual stresses and axial bending effects [1]. Asymmetric DV grooves can be employed to counteract undesirable bending by redistributing shrinkage through the thickness. BS 7910 presents profiles in the hoop and axial directions for DV groove applicable for both plate butt (girth) welds and axial seam welds. This is summarized in Table 3.1.

Table 3.1 Mapping between local weld directions (longitudinal and transverse) to pressure hull coordinate system (axial and circumferential/hoop).

Weld configuration	**Weld line orientation in hull**	**Local weld longitudinal direction**	**Local weld transverse direction**
Plating–web weld	Circumferential	Circumferential (hoop)	Axial
Web-flange weld	Circumferential	Circumferential (hoop)	Axial
Seam weld	Axial	Axial	Circumferential (hoop)
Girth weld	Circumferential	Circumferential (hoop)	Axial

4 Finite element modeling

The pressure hull considered in this study is referred to as "the Seahorse" and was originally presented in the paper by Reijmers et al. [16]. The same pressure hull geometry, together with its corresponding material parameters, was adopted in this thesis. In Reijmers work, the geometry was presented as the author's design and used as a representative submarine pressure hull geometry [16]. The Seahorse was selected for this thesis due to its relatively stiff ring stiffeners, making it suitable for studying interstiffener collapse, where yielding and collapse are primarily governed by the shell behavior between the stiffeners. The dimensions adopted are declared in Table 4.1 and illustrated in Figure 4.1. Reijmers et al. [16] also listed materials used for submarines. The considered materials were HY80 and HY100, two American high strength steels used for submarine pressure hulls. Both materials share the same elastic properties, with Young's modulus $E = 206$ GPa and Poisson's ratio $\upsilon = 0.3$. The yield stresses differ, however, and are 552 MPa for HY80 and 690 MPa for HY100 [16]. As presented in the previous section, four different weld configurations were considered: plating-web fillet welds, web-flange fillet welds, girth welds and seam welds. Additionally, cold bending in both the plating and the flanges were investigated.

Table 4.1: Dimensions of the considered pressure hull geometry, the Seahorse [16].

Hull length **L**	**Inner radius** **R**	**Hull thickness** **h**	**Stiffener spacing** $\mathbf{L_C}$	**Web height** $\mathbf{L_w}$	**Web thickness** $\mathbf{h_w}$	**Flange width** $\mathbf{L_f}$	**Flange thickness** $\mathbf{h_f}$
mm	mm	mm	mm	mm	mm	mm	mm
12150	3500	27	450	230	20	150	27

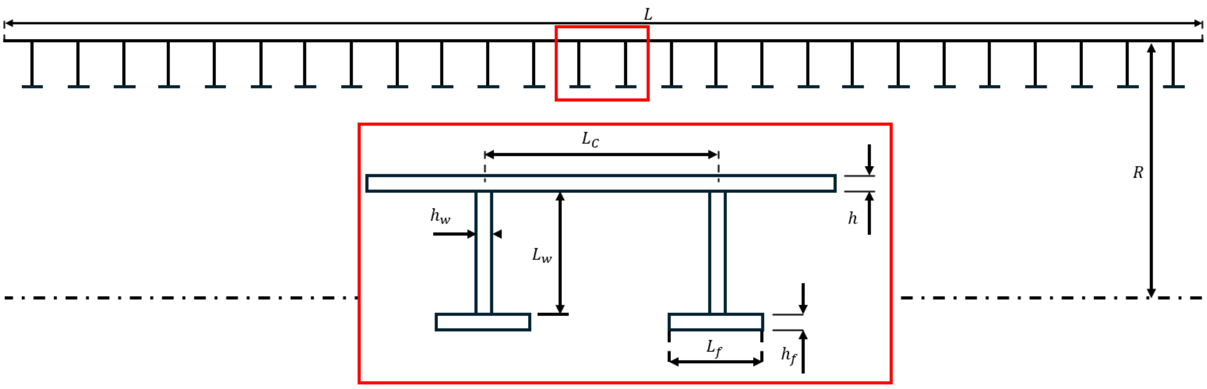

Figure 4.1: Illustration of the Seahorse mid-section pressure hull geometry and dimensions.

The study was divided into three parts:

i) Influence of individual residual stress sources on collapse pressure
ii) Investigation of the effect of weld width variation
iii) Study of the combined effect of residual stresses and cold bending and the influence of geometric imperfections

The analyses were performed on segments of the Seahorse pressure hull, using the geometry presented in Table 4.1. Three different finite element models of the Seahorse were considered: one model containing a single stiffener bay (the region between two stiffeners) and the other two containing three stiffener bays, all models have half bays at each end to accommodate the chosen boundary conditions later mentioned. Model 1 was used for the parametric study of individual residual stresses, whereas Models 2 and 3 were used in later studies. Models 2 and 3 were identical besides the different stiffener spacing and total length. Apart from different number of stiffener bays, identical boundary conditions, loading conditions and element set definitions were used in all models. All models are summarized in Table 4.2.

Table 4.2: Summary of the finite element models used in the study. All models are based on the Seahorse geometry, with Model 3 having increased stiffener spacing.

Model	**Hull length L**	**Stiffener spacing L_c**	**Number of full bays**	**Material**	**Element mesh size**	**Used in study**
	[mm]	[mm]	-	-	[mm]	
1	900	450	1	HY80	50	i)
2	1800	450	3	HY80, HY100	50	ii), iii)
3	2400	600	3	HY80, HY100	50	iii)

The nonlinear finite element analyses were performed using HyperMesh 2026.0.1 as pre-processor and Abaqus/Standard 2025 as solver. The analyses were performed using the implicit solver with a static general procedure with geometric nonlinearities. The material behavior is modelled as elastic-perfectly plastic, thereby introducing material nonlinearity into the analyses. For all models, the geometry was discretized using S8R and STRI65 shell elements, 8-node quadratic shell elements and 6-node quadratic triangular shell elements respectively, with nine through-thickness integration points. These shell elements have six degrees of freedom; three translational and three rotational per node. A cylindrical coordinate system was also adopted throughout the analyses.

A periodic boundary condition was selected to represent a segment of the Seahorse pressure hull far from bulkheads and additional boundary conditions constrain remaining rigid body movements, summarized in Table 4.3 and illustrated in Figure 4.2 a). To prevent rigid body translation and rotation in the cross-sectional plane two additional node pairs, denoted $\mathrm{BC_y}$ and $\mathrm{BC_z}$, were constrained in the y- and z-directions, respectively. These node pairs were chosen such that the coordinate of the direction they constrained was zero. For instance, $\mathrm{BC_y}$ nodes had the y-coordinate equal to zero, which gives a constrained rigid body motion without any artificial stresses or moments about those nodes. Together, these avoid artificial stress concentrations associated with overly restrictive constraints, while still allowing the model to capture the local structural response of the considered pressure hull segment.

An external pressure, p, was applied as a distributed load over the entire outer plating surface of the pressure hull. In addition, an axial compressive load corresponding to $N_x = p\frac{R}{2}$ [N/m] was applied as an edge load at the fore and aft end in accordance with thin-walled pressure vessel theory. The applied loads are illustrated in Figure 4.2 b).

Table 4.3: Node sets used for boundary conditions, the corresponding constrained degrees of freedom and their function.

Name	Constrained DOFs	Function	Purpose
BC_{aft}	1, 5, 6	Constrain axial translation and rotation about cross-sectional plane	Symmetry plane
BC_{fore}	5, 6	Constrain rotation about cross-sectional plane	Plane-section condition to be compatible with continuation with the hull but allow axial contraction
Kinematic coupling	1, 5, 6	Connect all nodes at the fore and ensure common axial translation	
BC_y	2	Constrain translation in the y-direction	Prevent rigid body motion
BC_z	3	Constrain translation in the z-direction	Prevent rigid body motion

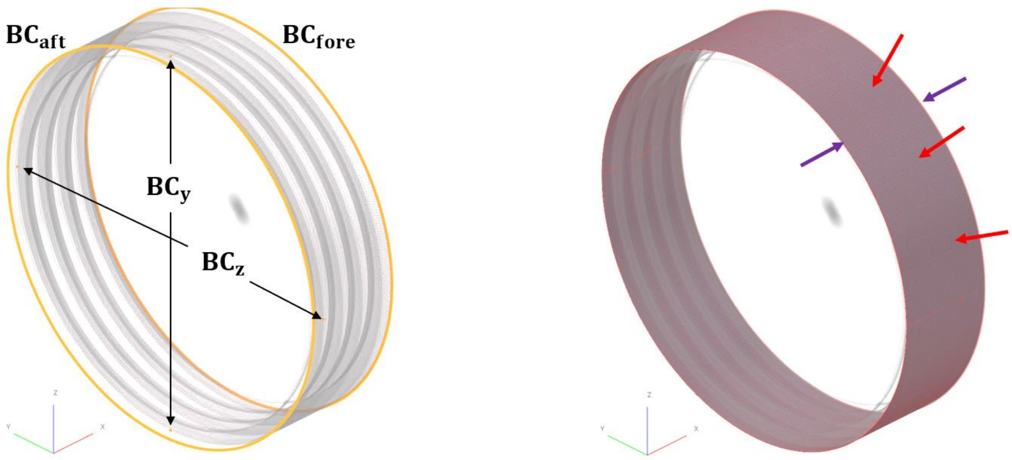

a) b)

Figure 4.2: a) Node sets used to define the boundary conditions in the Seahorse section geometry highlighted in yellow. b) Applied loads on the pressure hull, where the external pressure, p, and axial compressive load, N_x, by the red and purple arrows, respectively.

To evaluate the structural deformation induced by the residual stresses after relaxation, both radial deformation and axial shrinkage are presented. The bay deformations are measured at bays 1, 2 and 3 and denoted δ_w and δ_v for radial and axial deformation, respectively, as illustrated in Figure 4.3. In addition, the maximum radial displacement after relaxation, w_{max}, is used to describe the largest magnitude of the radial deformation caused by welding residual stress. All deformations are defined as positive for shrinkage.

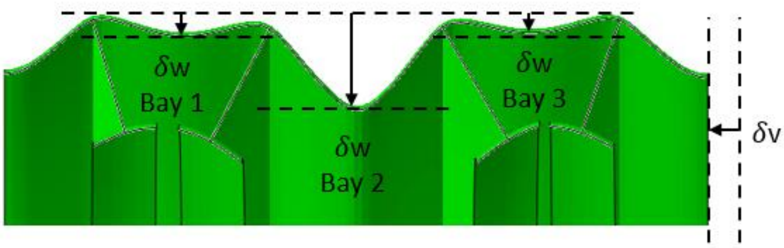

Figure 4.3. Deformation measures after residual stresses relaxation, where δ_w and δ_v represent the radial and axial deformation, respectively, defined as positive inward.

4.1 Residual stress modeling

To represent residual stresses arising from welding and cold bending, six different element sets were defined. An element set is a selection of the existing elements in the meshed geometry, allowing to distinguish between different regions within a component. These element sets included

- Cold bent plating (BP)
- Cold bent flanges (BF)
- Fillet welds between plating and web (FP)
- Fillet welds between web and flange (FF)
- Girth weld (G) (1/3 L_c from one ring stiffener)
- Seam welds (S)

The girth weld was placed 1/3 of the stiffener spacing from the ring stiffener, while five seam welds were used to encapsulate the pressure hull. Illustrations of the defined element sets on the model 2 with three and two half stiffener bays are presented in Figure 4.4.

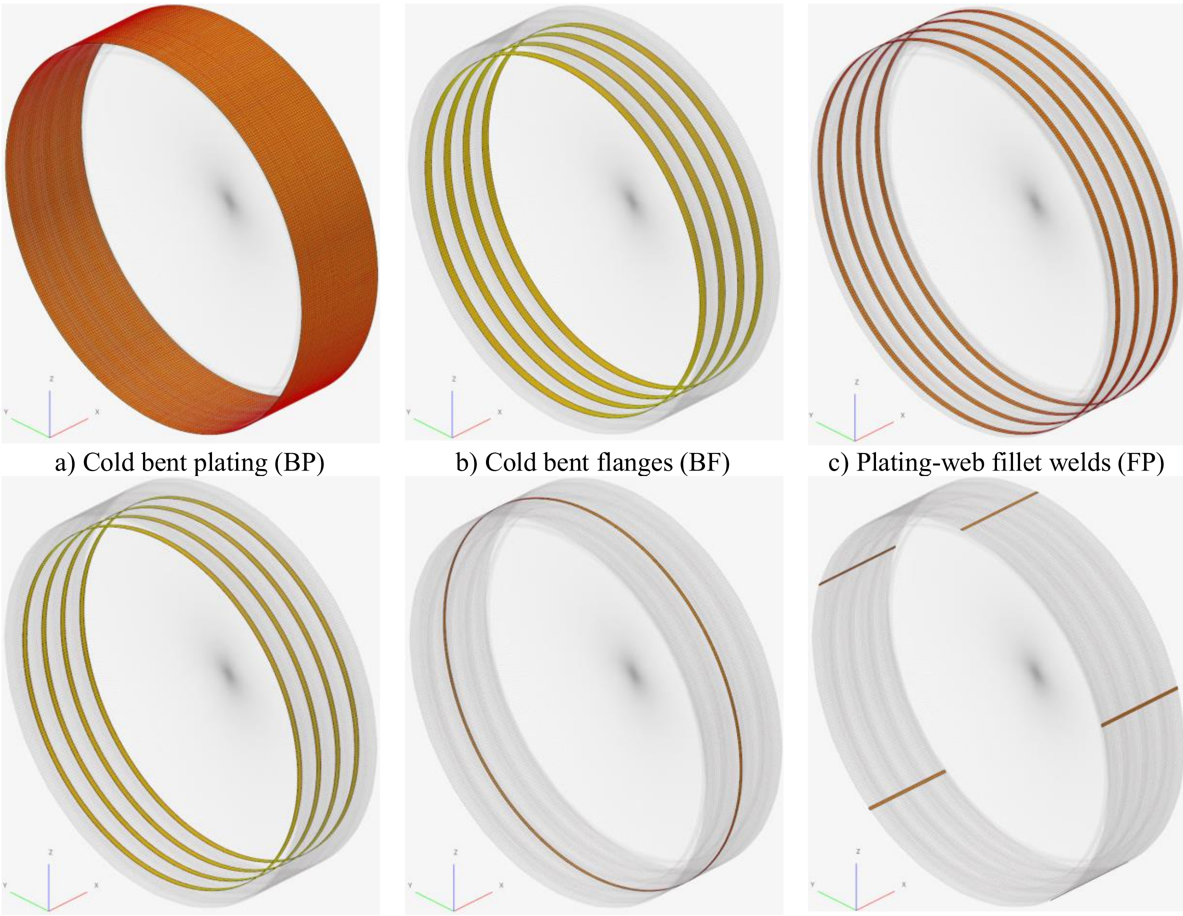

a) Cold bent plating (BP)
b) Cold bent flanges (BF)
c) Plating-web fillet welds (FP)
d) Web-flange fillet weld (FF)
e) Girth weld (G)
f) Seam welds (S)

Figure 4.4: Element sets defining the regions associated with the different manufacturing processes and the corresponding prescribed residual stress fields.

Residual stresses caused by welding were implemented using stress profiles obtained from BS 7910 and are presented in Table 4.4. Residual stresses caused by cold bending were calculated using the expressions presented in Equation (3.10). Once the residual stress distributions were established, the stress values at all nine integration points through the shell thickness were calculated using a developed Python script which extracted the correct value from the through-thickness residual stress profile based on each integration point's distance from the inner surface. The extracted curve from the script was then compared to the original stress profile from BS 7910 to ensure a correct representation. The residual stresses were introduced as initial stress conditions in Abaqus.

After assignment of the initial stress state, the model was allowed to reach equilibrium in a relaxation step, during which the residual stresses redistributed in accordance with the restraining structural stiffness, boundary conditions, and compatibility of the shell. The relaxation step also generates deformation of the structure as the initial residual stresses are not in equilibrium prior to the relaxation step. The resulting relaxed stress state and geometry then formed the starting point for the subsequent collapse analyses. A summarizing illustration of this procedure is shown in Figure 4.5 below.

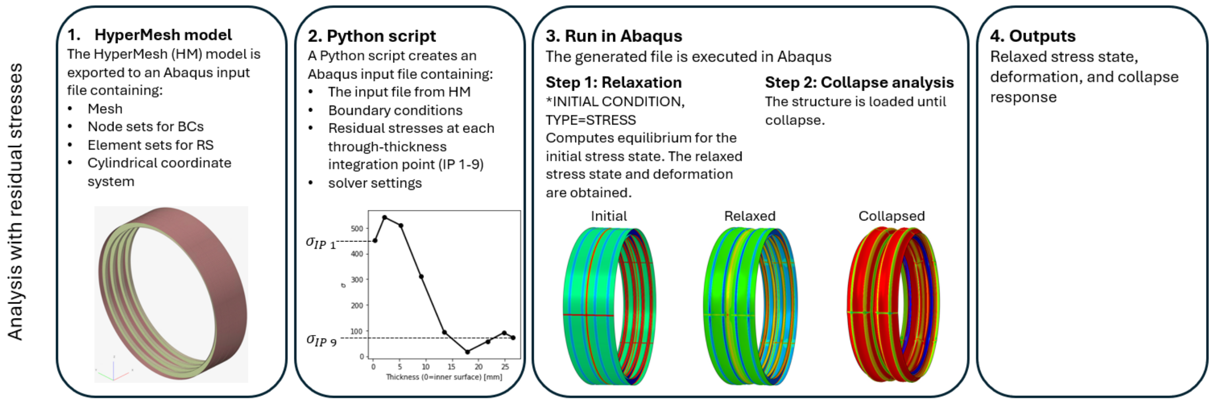

Figure 4.5: Workflow for implementation of residual stresses and collapse analysis.

In this thesis, collapse was defined as the onset of structural instability associated with loss of load carrying capacity in the response. Numerically, this was indicated by the instability of the static solver to continue the equilibrium path under increasing load, corresponding to the occurrence of a limit point or instability. The identified collapse point was not based on non-convergence alone but was confirmed through examination of the pressure-radial displacement plot response of the node with the largest radial displacement and the deformation and plastic development in the hull. Collapse was associated with a pronounced increase in radial displacement for only a small increase in pressure, together with the development of significant plastic strains through the thickness in the critical region.

Table 4.4: Residual stress components for fillet welds and plate butt welds with expressions from BS 7910 [15].

Plate-to-plate fillet welds		
Transverse stress		
$\frac{\sigma_m}{\sigma_y}$	$\frac{\sigma_b}{\sigma_y}$	$\frac{\sigma_{sb}}{\sigma_y}$
0.5	$0.5\left(\frac{z}{h}-\frac{1}{2}\right)$	0
Longitudinal stress		
$\frac{\sigma_m}{\sigma_y}$	$\frac{\sigma_b}{\sigma_y}$	$\frac{\sigma_{sb}}{\sigma_y}$
0.398	$0.543\left(\frac{z}{h}-\frac{1}{2}\right)$	$-0.1915 + 5.853\left(\frac{z}{h}\right) - 26.696\left(\frac{z}{h}\right)^2 + 38.11\left(\frac{z}{h}\right)^3 - 16.82\left(\frac{z}{h}\right)^4$

Plate butt welds: girth/seam welds		
Transverse/longitudinal stress		
$\frac{\sigma_m}{\sigma_y}$	$\frac{\sigma_b}{\sigma_y}$	$\frac{\sigma_{sb}}{\sigma_y}$
0.311	$0.289\left(\frac{z}{h}-\frac{1}{2}\right)$	$0.3415 + 5.8461\left(\frac{z}{h}\right) - 8.3994\left(\frac{z}{h}\right)^2 + 8.66\left(\frac{z}{h}\right)^3$
Longitudinal/transverse stress		
$\frac{\sigma_m}{\sigma_y}$	$\frac{\sigma_b}{\sigma_y}$	$\frac{\sigma_{sb}}{\sigma_y}$
0.767	$0.266\left(\frac{z}{h}-\frac{1}{2}\right)$	$-0.0829 + 2.037\left(\frac{z}{h}\right) - 8.287\left(\frac{z}{h}\right)^2 + 10.571\left(\frac{z}{h}\right)^3 - 4.08\left(\frac{z}{h}\right)^4$

4.2 Influence of individual residual stress sources on collapse pressure

For the parametric study, model 1 from Table 4.2 was employed with the boundary conditions and loads applied as previously described. The objective of the parametric study was to investigate how individual residual stress contributions influence the structural response of the pressure hull. Only one element set at a time was assigned an initial residual stress field, while remaining element sets were left unstressed. In this way, the influence of a specific weld type or cold bending on the structural collapse could be evaluated independently.

As discussed previously, the residual stress distribution is divided into three components: membrane, bending and self-balancing stresses. The study was performed by varying either the membrane or bending component as a fraction of the yield stress. The self-balancing component was first varied too, but as its influence on collapse pressure was rather small, it was set to the given expression from BS 7910 during this study. The residual stress is expressed according to

$$\sigma = \sigma_m + \sigma_b(z) + \sigma_{sb}(z)$$

where the membrane and bending component were varied separately as follows

$$\begin{cases} \sigma_m = x \cdot \sigma_y \\ \sigma_b = x \cdot \sigma_y \left(\frac{z}{h} - \frac{1}{2}\right) \\ x = [0.4, 0.6, 0.8, 1.0] \end{cases}$$

The stress components that were not varied were kept constant according to BS 7910, as presented in Table 4.4. To illustrate the procedure, the setups used for varying the membrane and bending components in the plating-web fillet weld are presented in Table 4.5 below. This was performed for all weld residual stress sources. For the girth weld, the profile was tested for both inwards and outwards bending to investigate its effect on the collapse pressure. The assumed weld width w_w was set to 50 mm for this study.

Table 4.5: Residual stress setup used to vary the membrane and bending component in the plating-web fillet weld for the parametric study.

Fillet plating (varying membrane component)		
Axial stress		
$\frac{x}{\sigma_y}$	$\frac{\sigma_b}{\sigma_y}$	$\frac{\sigma_{sb}}{\sigma_y}$
x = [0.4, 0.6, 0.8, 1.0]	$0.5\left(\frac{z}{h}-\frac{1}{2}\right)$	0
Hoop stress		
$\frac{x}{\sigma_y}$	$\frac{\sigma_b}{\sigma_y}$	$\frac{\sigma_{sb}}{\sigma_y}$
x = [0.4, 0.6, 0.8, 1.0]	$0.543\left(\frac{z}{h}-\frac{1}{2}\right)$	$-0.1915 + 5.853\left(\frac{z}{h}\right) - 26.696\left(\frac{z}{h}\right)^2 + 38.11\left(\frac{z}{h}\right)^3 - 16.82\left(\frac{z}{h}\right)^4$
Fillet plating (varying bending component)		
Axial stress		
$\frac{\sigma_m}{\sigma_y}$	$\frac{\sigma_b}{\sigma_y}$	$\frac{\sigma_{sb}}{\sigma_y}$
0.5	$x\left(\frac{z}{h}-\frac{1}{2}\right)$, x = [0.4, 0.6, 0.8, 1.0]	0
Hoop stress		
$\frac{\sigma_m}{\sigma_y}$	$\frac{\sigma_b}{\sigma_y}$	$\frac{\sigma_{sb}}{\sigma_y}$
0.398	$x\left(\frac{z}{h}-\frac{1}{2}\right)$, x = [0.4, 0.6, 0.8, 1.0]	$-0.1915 + 5.853\left(\frac{z}{h}\right) - 26.696\left(\frac{z}{h}\right)^2 + 38.11\left(\frac{z}{h}\right)^3 - 16.82\left(\frac{z}{h}\right)^4$

For the cold bending cases, the parametric study was carried out using the self-equilibrating Z-shaped residual stress profile defined by Equation (3.10). Rather than scaling the yield stress directly, the amplitude of the stress profile was varied such that the largest stress peak, σ_1 in Figure 3.2, corresponded to 0.4, 0.6, 0.8, and 1.0 times the yield stress, σ_y.

4.3 Investigation of the effect of weld width variation

In the present work, the weld width represents an assumed weld-affected region over which residual stresses are applied, rather than the physical fusion zone alone. Since this region is defined through the element sets, the assumed weld width directly affects internal forces F_i from the initial residual stresses applied through $F_i = \sigma \cdot A$, which relax in the first step. The purpose of this study was therefore to investigate how different choices of the weld-affected width influence the collapse pressure. To define a realistic range for the weld width w_w, lower and upper bounds were established based on geometric considerations and observations from the literature.

For the weld configurations considered in this work (fillet welds and DV grooves), the lower bounds were defined as

$$w_w = h_w/2 + \frac{h_w}{\sqrt{2}} \text{ (fillet weld)}$$

$$w_w = h \cdot \tan(\theta/2) \text{ (DV groove)}$$

where h_w is the web thickness, h is the plating thickness and θ is the groove angle.

The upper bound was based on the formulation by Faulkner [2], who describes the width of the tensile residual stress of fillet welds by $w_w = \eta h$, where η is a constant dependent on welding parameters and material properties. For ring stiffened structures, Faulkner suggests a value of $\eta = 1.5$. For the DV groove, the width of the entire groove is described by ηh. The lower and upper bounds for the two joints are illustrated in Figure 4.6.

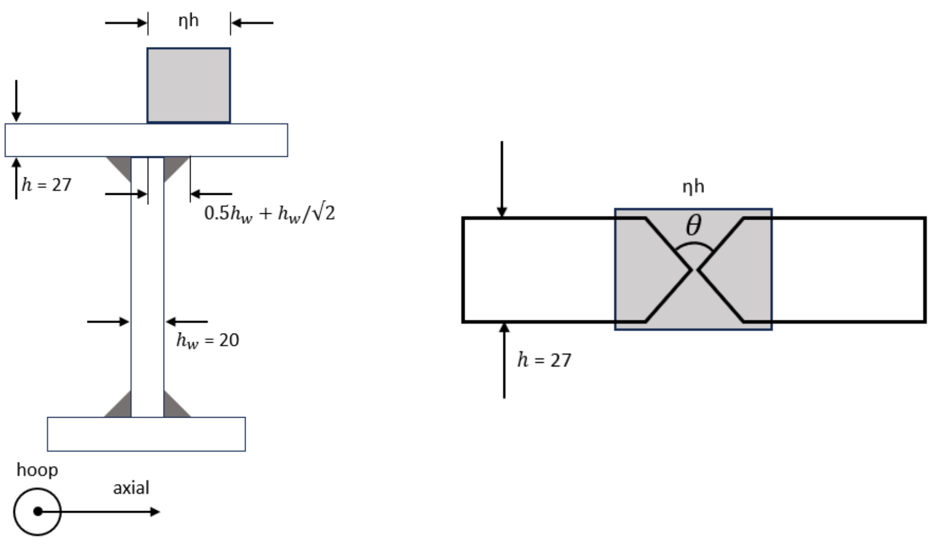

a) Fillet weld b) DV groove

Figure 4.6: Illustration of the lower and upper bounds for the assumed weld-affected width for a) fillet weld and b) DV groove.

The proposed bounds were assessed against experimental studies of fillet and DV groove welds with similar geometry and material properties [16, 17]. Comparisons with macrographs of the HAZ showed that geometric estimates were generally consistent with, or conservative relative to experimental observations. The geometric approach was therefore adopted as the lower bound.

Based on these bounds, three assumed weld widths (30, 40 and 50 mm) were selected for the study and applied to model 2, see Table 4.2. The prescribed weld widths were applied to the plating-web fillet weld, web-flange fillet weld and girth weld element sets. To represent the different weld-affected widths, partitions were introduced in the shell surfaces such that the geometry of the weld region corresponded to the three widths. The mesh was then generated on the partitioned geometry, which ensured that the weld-affected regions were represented consistently for the different cases. Residual stress profiles from BS 7910 and cold bending profiles were applied to the affected weld regions and the plating and flanges, respectively.

4.4 Combined residual stresses and geometric imperfections

In the combined residual stress study, all element sets and corresponding initial stress conditions were activated simultaneously, including cold bending in both the plating and flanges, plating-web and web-flange fillet welds, the girth weld and the seam weld. Unlike the parametric study, where each stress contribution was investigated separately, this study represents a more realistic condition in which all weld-induced residual stresses and cold bending effects were present simultaneously.

In addition to the combined residual stress field itself, the influence of stiffener spacing and material was also investigated by considering three cases. Case 1 corresponds to model 2 and HY80 steel, case 2 corresponds to model 3 and HY80 steel, and case 3 corresponds model 2 and HY100 steel. The corresponding geometries and model parameters are summarized in Table 4.2.

As in the previous analyses, the residual stress distributions were implemented according to the framework provided in BS 7910 and Table 4.4. Since BS 7910 stress profiles represent relaxed residual stress conditions in equilibrium with the restraining structure, the combined residual stress field for the first model was calibrated to achieve a similar relaxed stress distribution. This calibration was performed by scaling the residual stress magnitudes in the different weld element sets using multipliers of the yield stress. The calibrated multipliers are summarized in Table 4.6. With satisfactory calibration achieved for the first case, the same stress scaling factors were adopted for the remaining cases. Each case was then analyzed with rising external pressure until it collapsed.

Table 4.6: Calibrated multipliers used for the different element sets in the combined residual stress study to obtain a relaxed residual stress field similar to the BS 7910 profiles.

	Axial		**Hoop**	
	Membrane	**Bending**	**Membrane**	**Bending**
Plating-web fillet weld	-	-	0.7	0.8
Web-flange fillet weld	-	-	0.7	0.7
Seam weld	1.5	0.5	0.8	0.1
Girth weld			1.2	0.1

To investigate the influence of geometric imperfections on the collapse pressure, the relaxed displacement fields obtained from the combined residual stress analyses were imported into separate analyses as initial geometric imperfections. The geometric imperfection study was carried out for the same three cases considered in the combined residual stress study. For each case, the imperfect geometry was analyzed under increasing external pressure until collapse, and the results were compared with the corresponding analyses including the residual stress fields. Using this methodology, the influence of geometric imperfections arising from residual stress relaxation could be evaluated independently of the internal residual stress fields. This procedure is summarized in Figure 4.7.

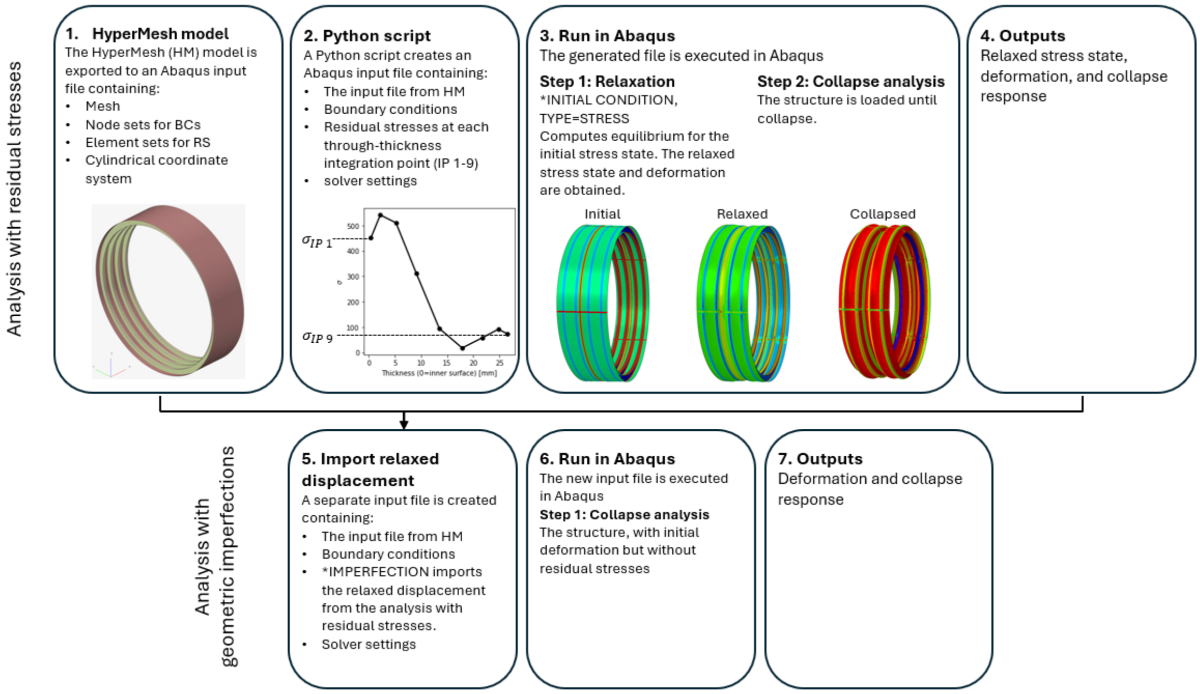

Figure 4.7: Workflow for implementation of geometric imperfections and collapse analysis.

5 Results

As residual stresses and imperfections are included in the analyses, an ideal stress-free analysis is created for the employed geometric and material models. Model 1 and 2 with HY80 material, identical to the structure by Reijmers et al. [16] but with a different number of stiffeners, have the same collapse pressure as reported in their paper. Model 2 with HY100 steel exhibits the same slope but can withstand a larger hydrostatic pressure before plastic collapse. Model 3 with HY80 steel exhibits a less stiff response and lower collapse pressure, expected from the changed geometry where the plating has a larger unsupported length between ring stiffeners. This is summarized in Table 5.1 and the corresponding pressure-displacement responses are shown in Figure 5.1.

Table 5.1. Reference pressures from plastic analyses on HY80 and HY100 for models 1, 2 and 3.

Model	**Material**	**Stiffener spacing [mm]**	**Plastic p_c [MPa]**
1, 2	HY80	450	6.79
2	HY100	450	8.13
3	HY80	600	5.83

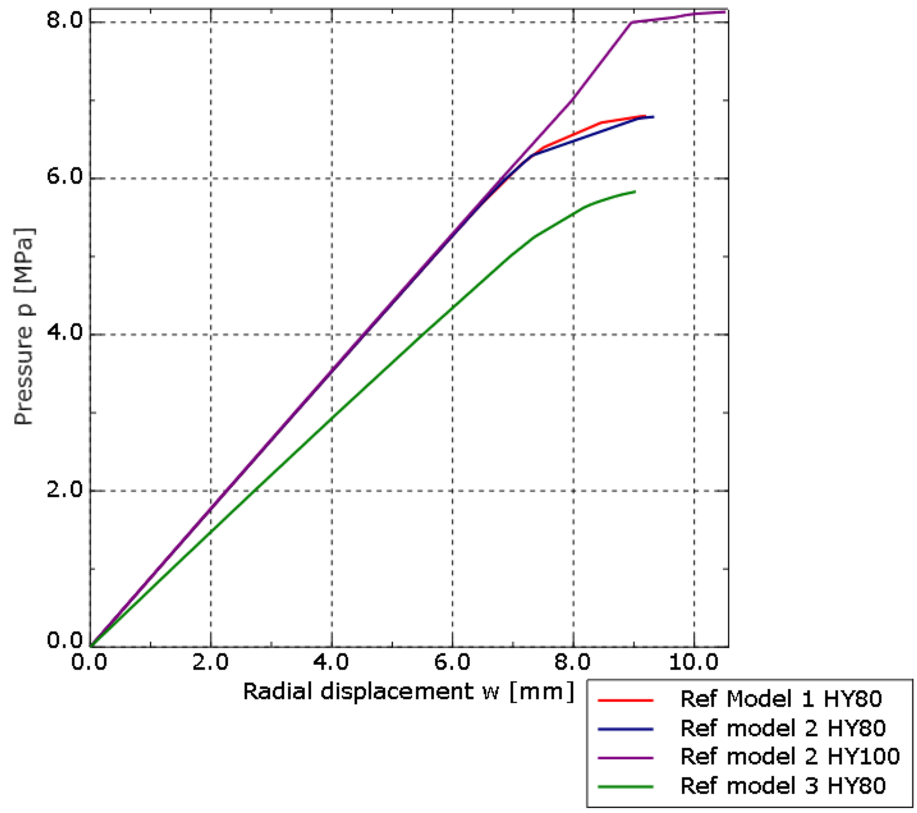

Figure 5.1: Pressure-displacement curves for the node with the largest radial displacement at collapse for models 1, 2 and 3 with HY80 and HY100.

5.1 Influence of individual residual stress sources on collapse pressure

The results of the parametric study are summarized in Figure 5.2 and provides an overall comparison of the investigated residual stress sources and identifies which contributions have the greatest influence on collapse pressure. The horizontal axis represents applied stress of the studied stress component expressed as a fraction of the yield stress, while the vertical axis shows the corresponding change in collapse pressure relative to the ideal reference analysis. The cold bent cases are shown as solid purple and pink lines. For the weld-induced residual stresses, the membrane stress variation is shown by solid lines, and the bending stress variation is shown as dashed lines. Additional results from the parametric study are presented in Appendix A.

Since the parametric study was performed by varying one residual stress component at a time, while the others were kept constant according to Table 4.5, each curve reflects not only the influence of the varied component but also the contribution from the fixed parts of the stress profile. Consequently, an indicator of the influence of the varied parameter is the slope of the curve, rather than the absolute level of collapse pressure reduction.

Figure 5.2 shows that the cold bending cases both exhibit a clear negative slope, indicating that increasing cold bending residual stress leads to a marked reduction in collapse pressure. Both membrane and bending stress for the plating-web fillet weld show a similar steep negative slope. The membrane component of the girth weld shows the largest reduction in collapse pressure, while the inward bending stress of the girth weld shows a smaller reduction. By contrast, the remaining tested stress components show nearly horizontal lines. The outward bending case for the girth weld is the only one that shows a slight increase in collapse pressure.

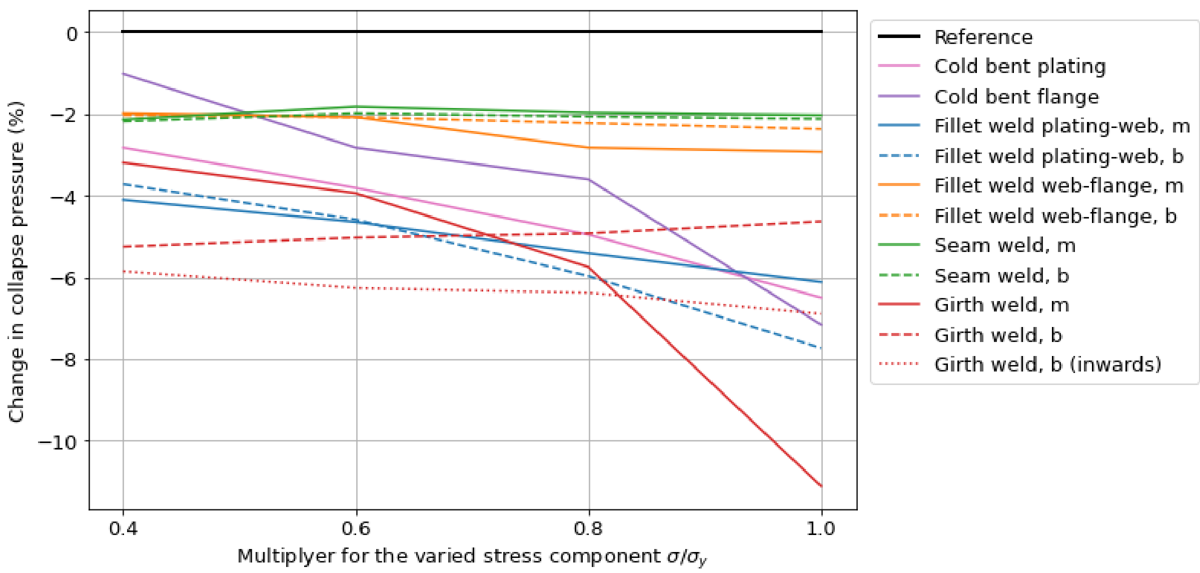

Figure 5.2: Parametric study of individual residual stress component's reduction on collapse pressure compared to an ideal reference analysis.

5.1.1 Influence of cold bending on collapse pressure

Figure 5.3 presents through-thickness residual stress distributions for the cold bent plating and flanges at the four investigated stress levels, with the collapse pressures and the relative reduction presented in Table 5.2. In both cases, the self-equilibrating Z-shaped profile is retained, while the amplitude increases with increasing x. Figure 5.4 shows that increasing cold bending residual stress reduces the collapse pressure for both the cold bent plating and cold bent flange cases. The effect is stronger for the plating than for the flange, as seen from the larger shift in the pressure-displacement response and the earlier onset of material yielding and continuous change in tangent stiffness (the slope in Figure 5.4).

Table 5.2: Results for the cold bent plating and flange cases including collapse pressure, and change in collapse pressure relative to the ideal, ideal reference analysis.

Cold bending	**Multiplier *x*:**	**0.0**	**0.4**	**0.6**	**0.8**	**1.0**
Plating	Collapse pressure p_c [MPa]	6.80	6.61	6.54	6.46	6.36
	Change from reference (%)	0.0	-2.8	-3.8	-5.0	-6.5
Flange	Collapse pressure p_c [MPa]	6.80	6.73	6.61	6.56	6.31
	Change from reference (%)	0.0	-1.0	-2.8	-3.5	-7.2

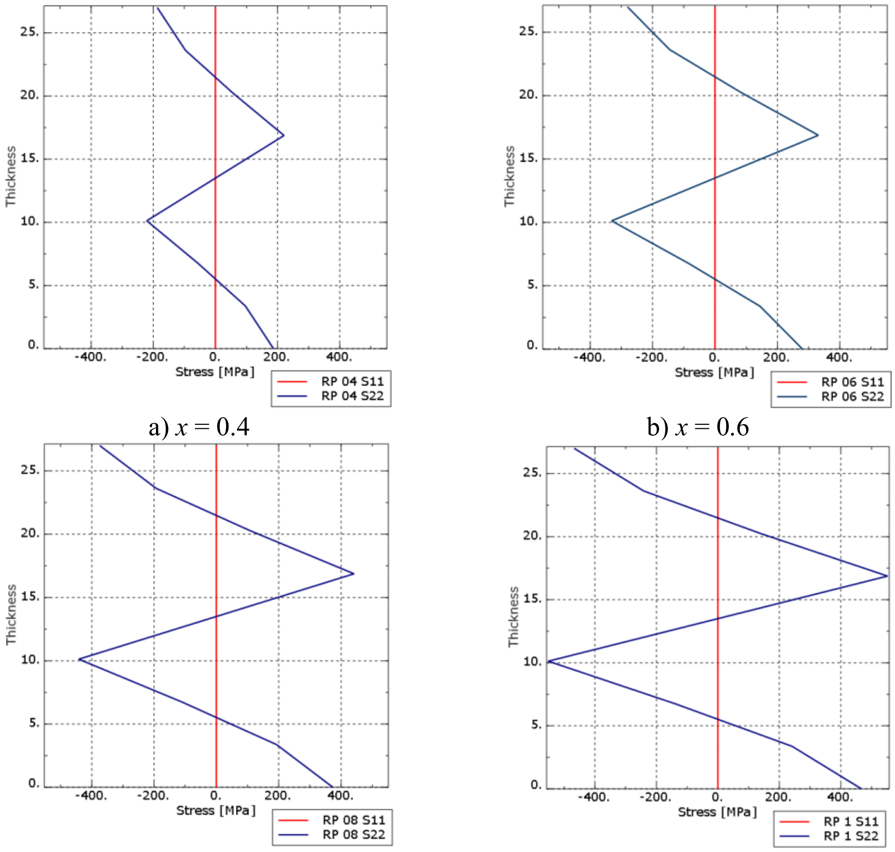

a) $x = 0.4$ b) $x = 0.6$

c) $x = 0.8$ d) $x = 1.0$

Figure 5.3: Through-thickness residual stress profiles for both the cold bent plating and the cold bent flange. The vertical axis shows the thickness of the material [mm], 0 is the inside surface of the plating. The horizontal axis shows stress [MPa]. Only the relaxed profile is shown, since it is in self-equilibrium, and does not change after relaxation. Red indicates axial stress ($S11$) and blue indicates hoop stress ($S22$).

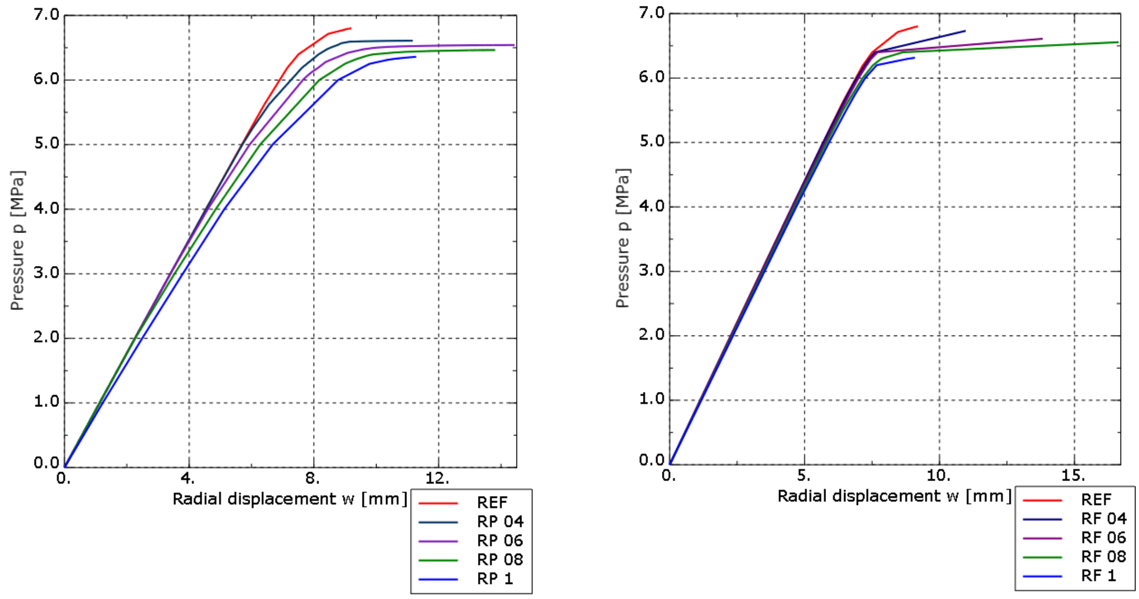

a) b)

Figure 5.4: Radial pressure-displacement plots for the cold bent a) plating (RP) and b) flange (RF) with the stress ideal reference analysis and the four tested stress levels, respectively.

5.1.2 Influence of plating-web fillet weld on collapse pressure

The relaxed radial deformation and axial shrinkage for the plating-web fillet weld is summarized in Table 5.3. For the membrane stress variation, δ_w remains nearly constant, while $w_{\max}$ and δ_v increases with increasing x. Varying the bending stress shows that δ_w increases with x but δ_v remains constant.

Figure 5.6 shows representative through-thickness stress profiles for the varied membrane and bending stress components, together with the corresponding relaxed midbay response. For the membrane variation, the axial stress component relaxes to nearly the same profile for all investigated multipliers, both in the weld region and at midbay but results in different magnitude of axial shrinkage δ_v. The hoop membrane stress, however, relaxes only partially, resulting in a larger residual stress state after relaxation as the stress level increases. The midbay response further shows that increasing hoop membrane stress at the weld leads to increased compressive stress at midbay after relaxation. For the bending variation, the profile relaxes to stress profiles with higher tensile stress with increased bending stress. The response midbay is also increased with x.

The corresponding pressure-displacement curves are shown in Figure 5.5. For both the membrane and bending stress variations, increasing stress magnitude leads to a reduction in collapse pressure compared with the ideal reference analysis. The effect is more pronounced for the bending component, which produces a clearer downward shift of the pressure-displacement curve, deviating from the reference path. The membrane component shows the same overall trend, although with a smaller reduction in collapse pressure.

Table 5.3: Measured collapse pressure and deformation measurements after relaxation for the varied membrane and bending stress in the plating-web fillet weld.

Varied parameter	**Multiplier:**	**0.0**	**0.4**	**0.6**	**0.8**	**1.0**
Membrane	Collapse pressure p_c [MPa]	6.80	6.52	6.49	6.43	6.38
	Change from reference (%)	0.0	-4.1	-4.6	-5.4	-6.1
	w_{max} [mm]	0.0	0.58	0.73	0.87	1.01
	δw [mm]	0.0	0.36	0.35	0.33	0.32
	δv [mm]	0.0	0.15	0.23	0.32	0.40
Bending	Collapse pressure p_c [MPa]	6.80	6.55	6.49	6.40	6.28
	Change from reference (%)	0.0	-3.7	-4.6	-6.0	-7.7
	w_{max} [mm]	0.0	0.50	0.60	0.71	0.82
	δw [mm]	0.0	0.28	0.44	0.59	0.75
	δv [mm]	0.0	0.20	0.20	0.20	0.20

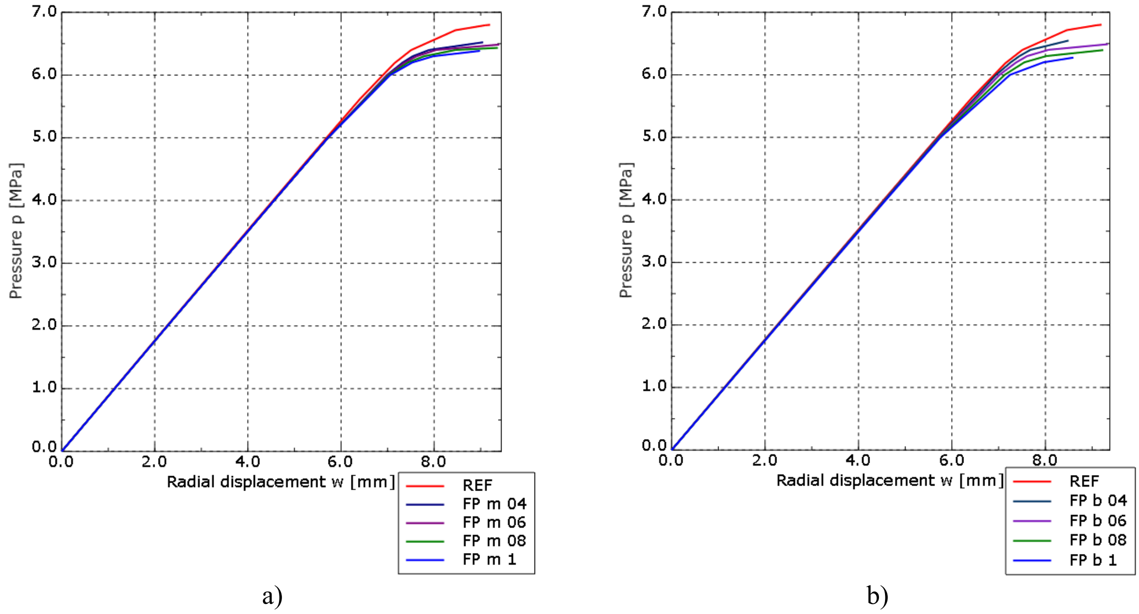

Figure 5.5: Pressure-displacement curves for the plating-web fillet weld with varied a) membrane stress component (FP_m) and b) bending stress component (FP_b), shown together with the ideal reference analysis and the four investigated stress levels.

Plating-web fillet weld

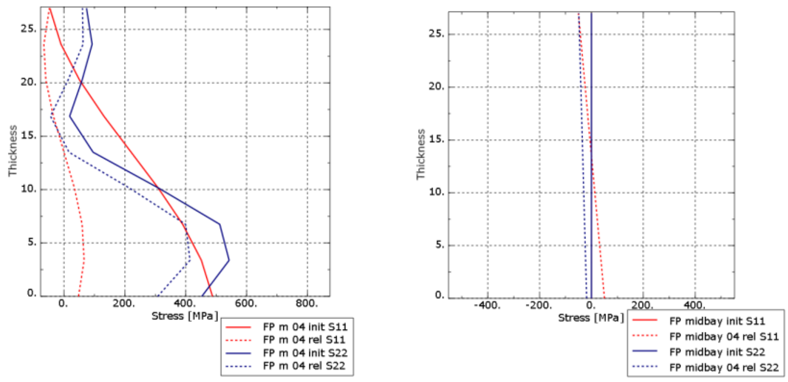

a) $x = 0.4$

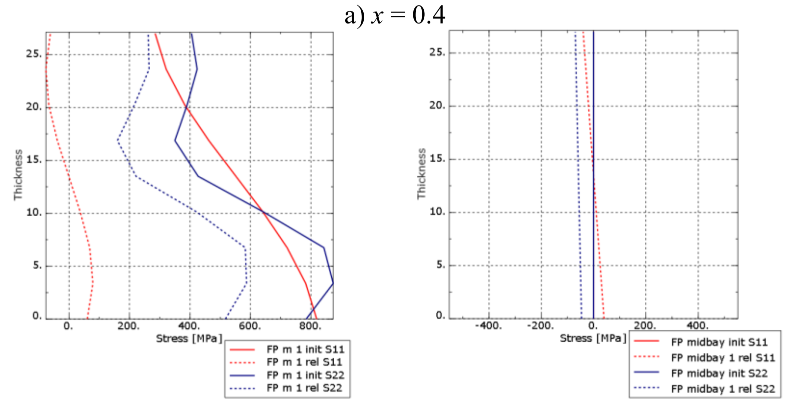

b) $x = 1.0$

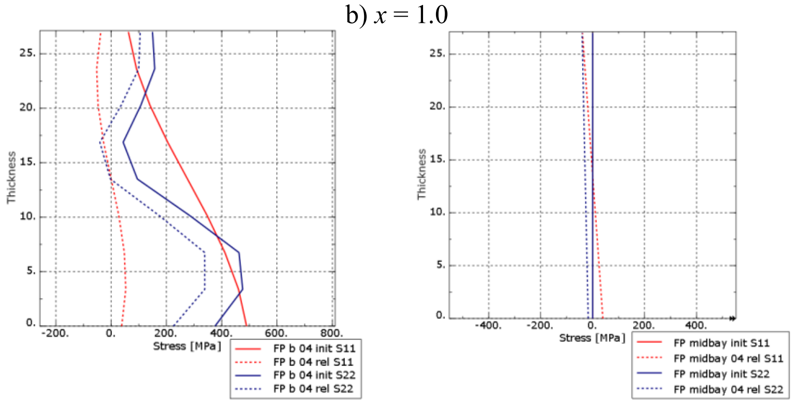

c) $x = 0.4$

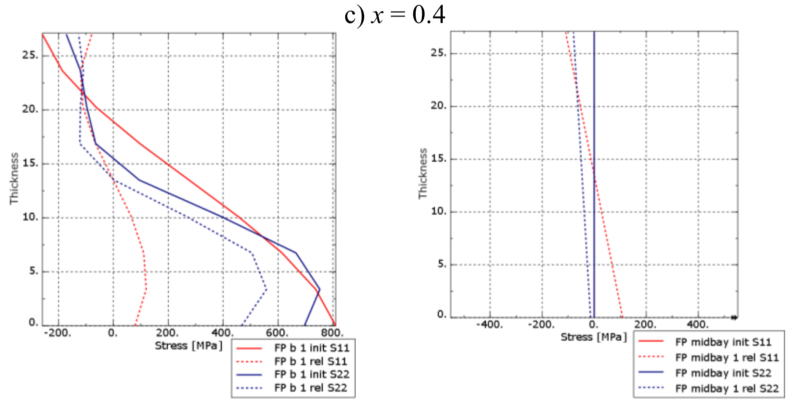

d) $x = 1.0$

Figure 5.6: Left column: through-thickness residual stress profiles in the plating-web fillet weld, FP, for a), b) varied membrane stress component and c), d) varied bending stress component. Right column: corresponding midbay responses. The vertical axis represents the material thickness (mm), with 0 at the inner plating surface. The horizontal axis represents stress (MPa). Solid lines indicate the initial residual stress state, dashed lines indicate the relaxed stress profile. Red denotes axial stress (S_{11}) and blue denotes hoop stress (S_{22}).

5.1.3 Influence of the girth weld on collapse pressure

The relaxed deformation in Table 5.3 indicates that the membrane stress component leads to a gradual increase in both radial deformation, δw, and axial shrinkage, δv, as the stress multiplier x increases. The outward bending produces only limited axial shrinkage and a varying radial response. For higher stress levels, the radial deformation becomes outward, resulting in a negative δw. Inward bending leads to a pronounced increase in radial deformation, while δv remains essentially constant.

Representative through-thickness stress profiles are shown in Figure 5.7 for the membrane and inward bending cases. For both the membrane stress variation and the inward bending stress variation, the axial stress relaxes to a similar stress profile within the weld region for the respective case. The highest compressive stress is in the center of the hull plating at about -180 MPa and tensile stress near the surfaces. The hoop stress only partially relaxes.

The pressure-displacement curves corresponding to the girth weld tests are shown in Figure 5.8. Varying the membrane stress shows the largest decrease in collapse pressure, while the inward bending only shows slight decrease in collapse pressure with increased x. On the contrary, outward bending shows a slight increase in collapse pressure with larger x. All inward bending variations show the earliest deviation from the reference path.

Table 5.4: Calculated collapse pressure and relaxed deformation for the varied membrane stress and outward and inward bending stress components in the girth weld.

Varied parameter	**Multiplier:**	**Ref**	**0.4**	**0.6**	**0.8**	**1.0**
Membrane	Collapse pressure p_c [MPa]	6.80	6.58	6.53	6.41	6.05
	Change from reference (%)	0.0	-3.2	-3.9	-5.7	-11.0
	w_{max} [mm]	0.0	0.11	0.19	0.28	0.38
	δw [mm]	0.0	-0.029	0.050	0.093	0.14
	δv [mm]	0.0	0.054	0.075	0.096	0.12
Outward bending	Collapse pressure p_c [MPa]	6.80	6.44	6.46	6.47	6.49
	Change from reference (%)	0.0	-5.3	-5.0	-4.9	-4.6
	w_{max} [mm]	0.0	0.32	0.27	0.24	0.26
	δw [mm]	0.0	0.063	-0.055	-0.18	-0.30
	δv [mm]	0.0	0.034	0.035	0.035	0.036
Inward bending	Collapse pressure p_c [MPa]	6.80	6.40	6.38	6.37	6.33
	Change from reference (%)	0.0	-5.9	-6.2	-6.3	-6.9
	w_{max} [mm]	0.0	0.64	0.75	0.86	0.96
	δw [mm]	0.0	0.42	0.53	0.64	0.75
	δv [mm]	0.0	0.034	0.034	0.034	0.034

Girth weld

Varied membrane stress

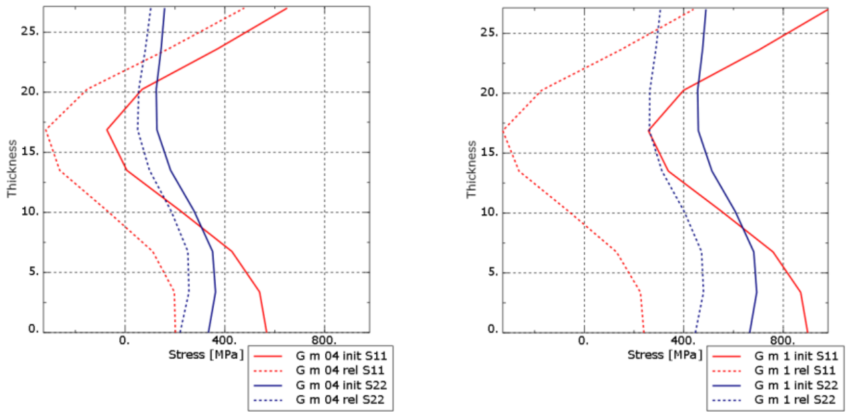

a) $x = 0.4$ b) $x = 1.0$

Varied inward bending stress

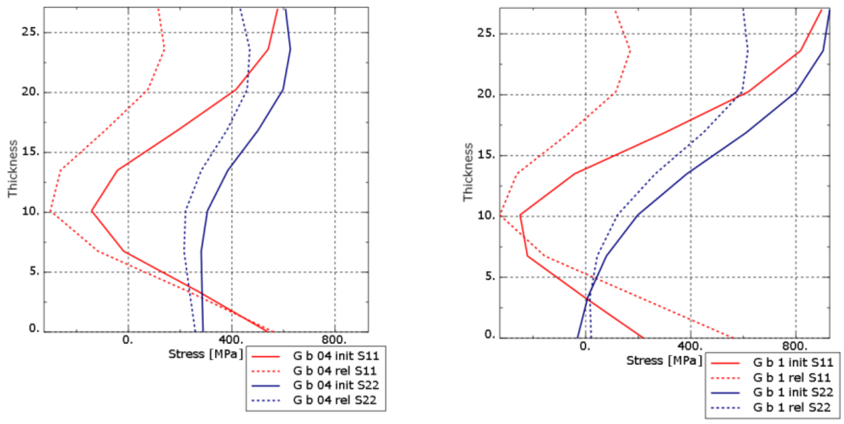

c) $x = 0.4$ d) $x = 1.0$

Figure 5.7: Through-thickness residual stress profiles for the girth weld, G, for a) and b) varied membrane stress component and c) and d) varied bending stress component. The vertical axis represents the material thickness (mm), with 0 at the inner plating surface. The horizontal axis represents stress (MPa). Solid lines indicate the initial residual stress profile, dashed lines indicate the relaxed stress profile. Red denotes axial stress (S_{11}) and blue denotes hoop stress (S_{22}).

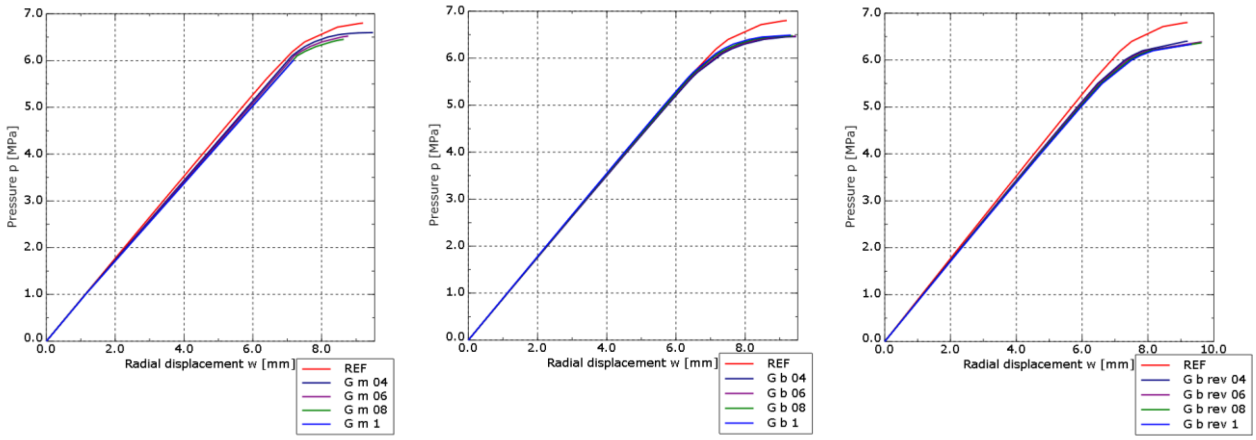

a) pressure-displacement plot for varied membrane stress

b) pressure-displacement plot for different outward bending

c) pressure-displacement plot for different inward bending

Figure 5.8: Pressure-displacement curves for the girth weld with varied a) membrane stress component (G_m), b) bending stress component ($G_{b,outward}$), and c) bending stress component ($G_{b,inward}$), shown together with the ideal reference analysis and the four investigated stress levels.

5.2 Investigation of the effect of weld width variation

Table 5.5 summarizes the collapse pressure and the corresponding radial and axial deformation after relaxation for the three investigated cases with applied stress profiles from BS 7910 and varied width of the assumed weld affected zone. The collapse pressure decreases slightly with increasing assumed weld width, from 6.35 MPa for 30 mm to 6.28 MPa for 50 mm, corresponding to a reduction of approximately 5.1% and 6.0% respectively, relative to the respective reference case. The table with radial deformation paired with the contour plots with radial displacement after relaxation, shown in Figure 5.9, shows that w_w = 50 mm has the largest total deformation and largest δ_w, which decreases with smaller w_w. The pressure-displacement response for the three prescribed widths are presented in Figure 5.10.

Table 5.5. Results of the weld width variation including collapse pressure, radial and axial deformation.

Weld width w_w [mm]	**Ref p_c [MPa]**	**p_c [MPa]**	**Change [%]**	**δ_w [mm] Bay 1**	**δ_w [mm] Bay 2**	**δ_w [mm] Bay 3**	**δ_v [mm]**
30	6.69	6.35	-5.1	0.27	0.45	0.23	0.25
40	6.65	6.33	-4.8	0.35	0.59	0.29	0.33
50	6.68	6.28	-6.0	0.41	0.71	0.34	0.41

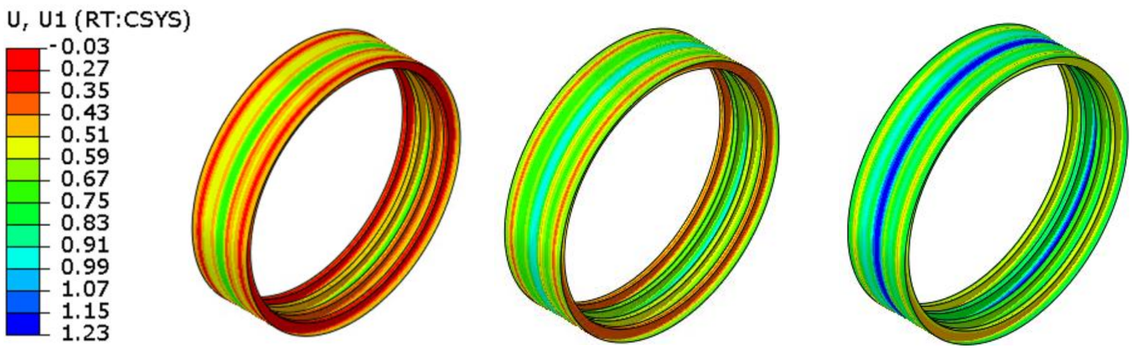

w_w = 30 mm w_w = 40 mm w_w = 50 mm

Figure 5.9. Radial deformation after relaxation for weld width 30 mm, 40 mm and 50 mm, respectively. Deformation is defined as positive inwards [mm], scaled 25 times.

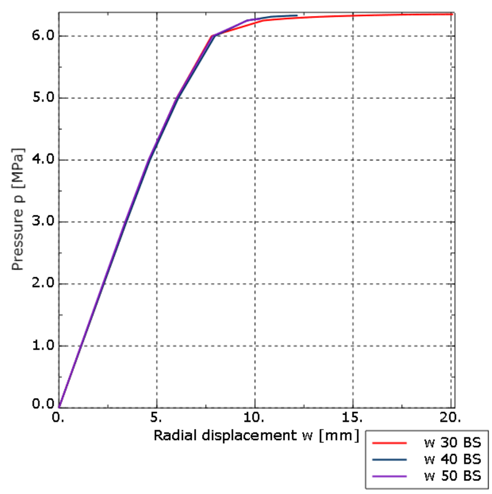

Figure 5.10. Pressure-displacement curve for weld widths 30, 40 and 50 mm. Applied residual stress fields from BS 7910.

5.3 Investigation of the combined effect of residual stresses and geometric imperfections

Next, the combined effect of residual stresses applied to all element sets together with cold bending in both the plating and flanges is investigated. Note that in the combined case, the bending of the girth weld is placed outwards. In addition, the influence of solely initial geometric imperfections from the residual stress relaxation is evaluated and compared to the effect of residual stress. In this section, the collapse pressures and the deformation after relaxation for the ideal reference analysis, residual stress analysis and imperfect analysis are presented. Pressure-displacement curves are presented for the node subjected to the largest radial displacement and finally contour plots of the hoop and von Mises stress distributions at collapse of the reference, residual stress and imperfect analyses.

Table 5.6 presents the collapse pressures obtained from the plastic reference analysis, the residual stress analysis and the geometric imperfect analysis for all cases. The percentage reduction in collapse pressure relative to the ideal reference analyses is also included. In Table 5.6 it is observed that the reduction in collapse pressure is smaller for the imperfect analysis than for the analysis which include the applied residual stresses. However, the overall collapse pressures are lower for Case 2 which has a stiffener spacing of L_c = 600 mm, compared to Case 1 which has a stiffener spacing of L_c = 450 mm. In addition, the use of HY100 steel (Case 3), results in higher collapse pressures compared to the corresponding HY80 cases (Case 1 and Case 2).

Table 5.6. Collapse pressures for the plastic reference analysis, the model with applied residual stresses and the imperfect case with initial geometric imperfections for Case 1, Case 2 and Case 3. Radial and axial deformations (after relaxation) and maximum radial deformation at relaxation are also presented for the residual stress model.

Case			p_c	Change	w_{max}	δ_w			δ_v
						Bay 1	Bay 2	Bay 3	
			MPa	%	mm		mm		mm
1	HY80 450mm	Plastic reference	6.79	0.0	0.0	0.0	0.0	0.0	0.0
		Residual stresses	6.04	-11.0	2.3	0.36	0.90	0.24	0.35
		Imperfect	6.33	-6.8	2.3	0.36	0.90	0.24	0.35
2	HY80 600mm	Plastic reference	5.83	0.0	0.0	0.0	0.0	0.0	0.0
		Residual stresses	5.22	-10.5	2.2	0.12	0.89	0.082	0.35
		Imperfect	5.54	-5.0	2.2	0.12	0.89	0.082	0.35
3	HY100 450mm	Plastic reference	8.13	0.0	0.0	0.0	0.0	0.0	0.0
		Residual stresses	6.94	-14.6	2.9	0.45	1.1	0.34	0.44
		Imperfect	7.70	-5.3	2.9	0.45	1.1	0.34	0.44

Pressure-displacement curves are shown in Figure 5.11 for Case 1, Case 2 and Case 3. Each subfigure compares the plastic reference analysis, the analysis with residual stress and the analysis with geometric imperfections. The imperfect cases generally follow the reference response more closely before deviating at higher pressures, resulting in collapse pressures between those of the reference and residual stress analyses. The results further show that increasing stiffener spacing leads to larger deformations and reduced collapse resistance, whereas the use of higher-strength steel increases the overall collapse pressure. For all cases, the residual stress model exhibits the earliest deviation from the reference analysis, followed by a more pronounced nonlinear response and lower collapse pressures.

In Case 1, shown in Figure 5.11 a), the curves initially follow a similar response up to slightly above 3 MPa. Beyond this point, the residual stress analysis deviates from the reference analysis and flattens until plastic collapse occurs at approximately 6 MPa. The imperfect case also deviates near this pressure level, although to a lesser extent, and remains nearly parallel to the reference curve before collapsing at approximately 6.3 MPa.

Case 2 shows trends similar to Case 1, see Figure 5.11 b). Both cases employ HY80, although Case 2 has a larger stiffener spacing. In the pressure-displacement response, all three curves remain close to approximately 3 MPa, after which the residual stress model deviates from the reference analysis. Compared to Case 1, the residual stress curve develops a flatter nonlinear response and collapses earlier, at approximately 5.2 MPa. This reduction in collapse pressure is accompanied by larger radial deformations.

In Case 3, HY100 is used instead of HY80. In the pressure-displacement curve in Figure 5.11 c), the residual stress model begins to deviate from the reference analysis at approximately 4 MPa and collapses at nearly 7 MPa. The imperfect case also deviates near 4 MPa but continues approximately parallel to the reference before collapsing at about 7.7 MPa.

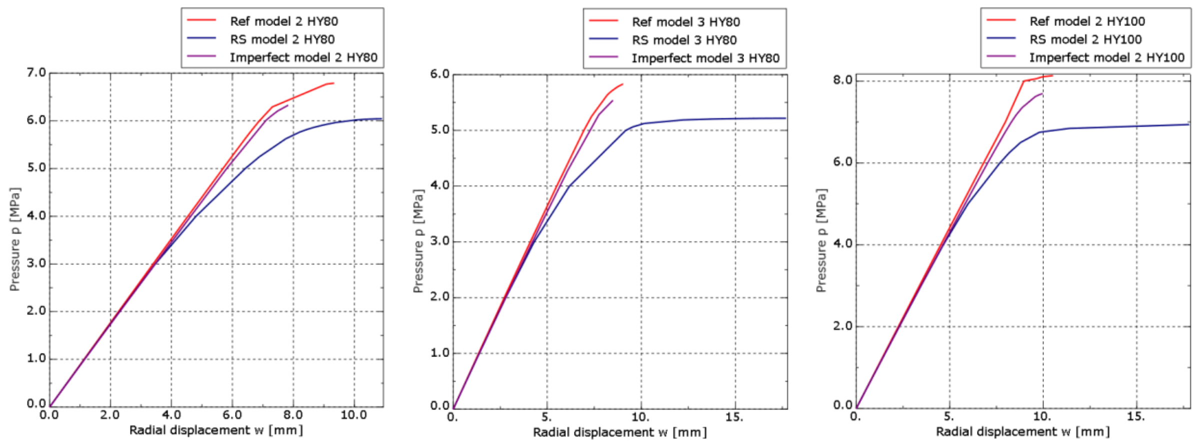

a) Case 1 b) Case 2 c) Case 3

Figure 5.11. Pressure-displacement curves for the node exhibiting the largest radial displacement for Case 1 (HY80, L_c = 450 mm), Case 2 (HY80, L_c = 600 mm) and Case 3 (HY100, L_c = 450 mm) including reference, residual stress and imperfect analysis. The vertical axis represents the radial displacement [mm] and the horizontal axis represents the pressure [MPa].

The hoop and von Mises stress distributions in a quarter-section cut in the y- and z-plane at the final load step are investigated for Case 1, Case 2, and Case 3, see Figure 5.12, Figure 5.14 and Figure 5.13. Subfigures a) and b) show the contour plots for the analysis including residual stress, while subfigures c) and d) correspond to the analysis with only the relaxed geometric imperfections. The contour plots also indicate tripping of the stiffeners, although the deformation shapes are amplified by the applied scaling factor. The collapse is however governed for case 1 and 2 by through-thickness plastic strain in bay 2, which is seen in the corresponding von Mises stress plots, Figure 5.12 b) and Figure 5.13 b), where both the outside and inside surface have reached the yield stress.

Examining the results reveals similar trends between the cases. For the residual stress analysis, the hoop stress distributions show compressive stresses in all regions apart from the fillet weld and seam weld associated element sets, while the girth welds are loaded to compressive stresses. For the imperfect case, the hoop stress contour plots show compressive stresses throughout the entire model, see Figure 5.12 c), Figure 5.14 c) and Figure 5.13 c). The largest compressive stresses are observed in the plating, while smaller compressive stresses occur in the fillet welds and ring stiffeners.

The von Mises stress distributions for the residual stress cases in Figure 5.12 b), Figure 5.13 b) and Figure 5.14 b) show that yielding occurs throughout most of the outer plating, except in the regions near the fillet welds between the plating and web. For the residual stress analyses, the girth weld also exhibits lower von Mises stress magnitudes. For Case 1 and Case 2, especially Case 2, the yield stress is reached in the midbay region, both in the inner and outer parts, indicating full development of plastic strain of the cross-section. For case 3, the development of through-thickness plastic strain only reaches 3/4 of the thickness from the outer surface. For the cases with geometric imperfections, the outer plating, excluding the stiffener regions, has largely reached the yield limit. However, yielding in the midbay region is not as clear for the imperfect cases as for the residual stress cases.

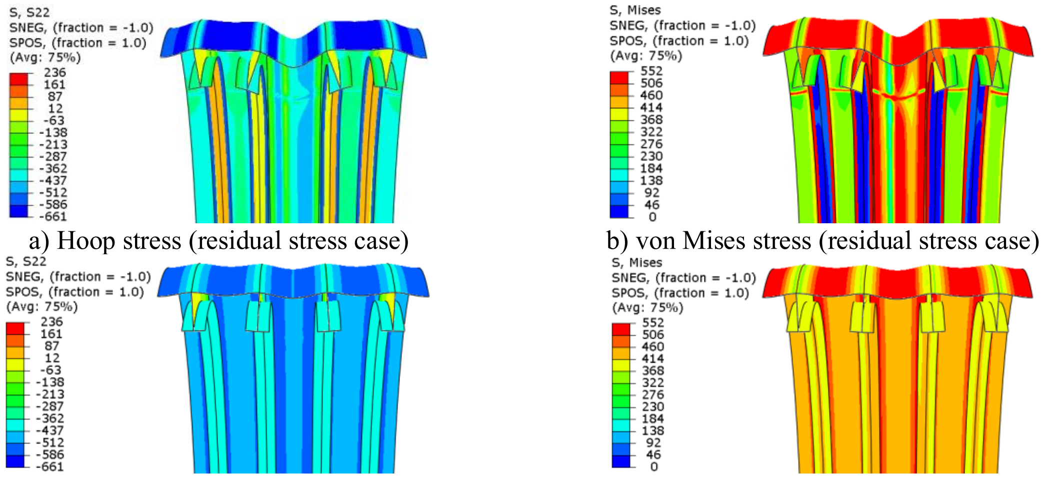

a) Hoop stress (residual stress case) b) von Mises stress (residual stress case)

c) Hoop stress (imperfect case) d) von Mises stress (imperfect case)

Figure 5.12. Contour plots for Case 1 (HY80, L_c = 450 mm) for the last converged load step with a scaling factor of 25. Subfigures a) and b) show the hoop and von Mises stress for the residual stress model, respectively, while c) and d) show the contour plots for the imperfect case.

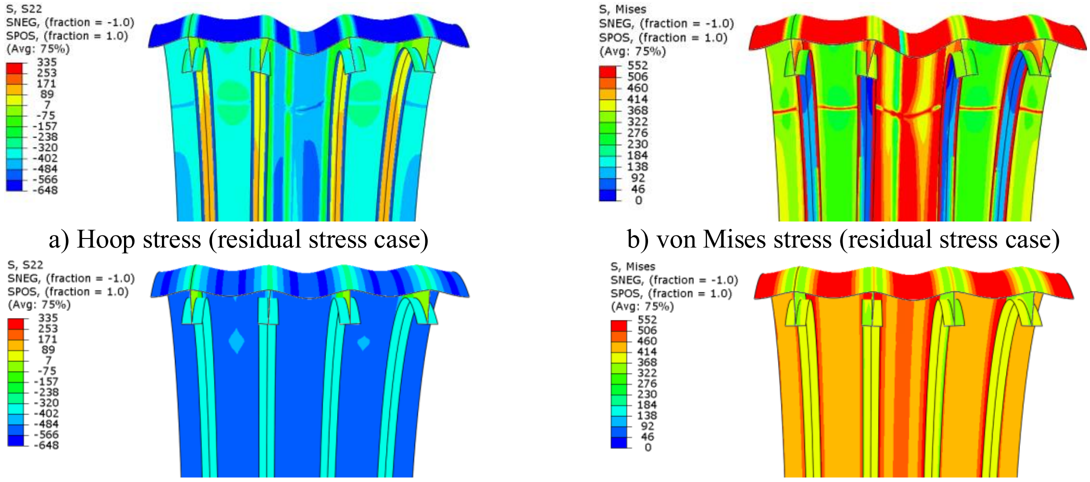

a) Hoop stress (residual stress case) b) von Mises stress (residual stress case)

c) Hoop stress (Imperfect case) d) von Mises stress (imperfect case)

Figure 5.13. Contour plots for Case 2 (HY80, L_c = 600 mm) for the last converged load step with a scaling factor of 25. Subfigures a) and b) show the hoop and von Mises stress for the residual stress model, respectively, while c) and d) show the contour plots for the imperfect case.

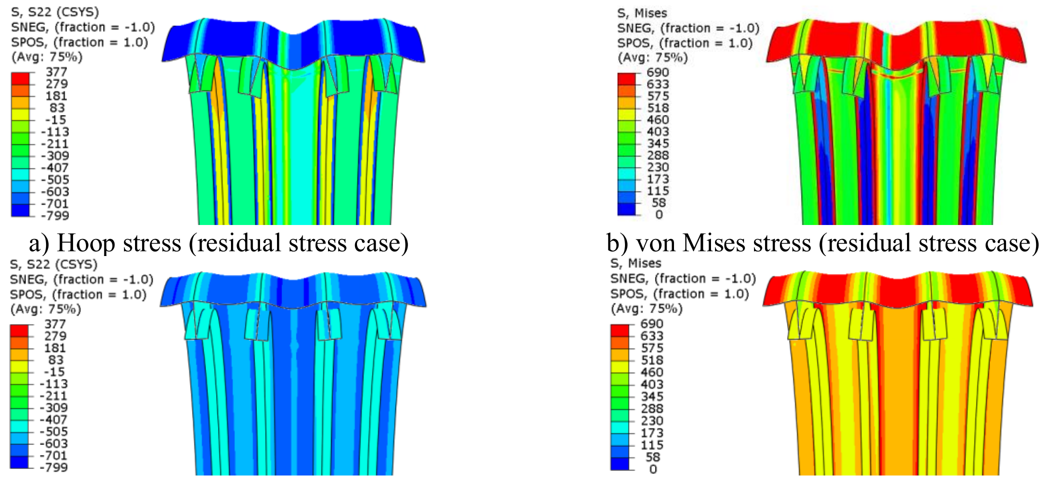

a) Hoop stress (residual stress case) b) von Mises stress (residual stress case)

c) Hoop stress (imperfect case) d) von Mises stress (imperfect case)

Figure 5.14. Contour plots for Case 3 (HY100, L_c = 450 mm) for the last converged load step with a scaling factor of 25. Subfigures a) and b) show the hoop and von Mises stress for the residual stress model, respectively, while c) and d) show the contour plots for the imperfect case.

6 Discussion

This chapter discusses the results presented in Chapter 5 with respect to the influence of residual stresses and geometric imperfections on the collapse behavior of a ring stiffened submarine pressure hull subjected to external pressure. The discussion is structured according to the main objectives of the thesis: the effect of individual residual stress sources, the effect of combined residual stress sources, the relative importance of residual stresses and geometric imperfections and the underlying mechanism by which residual stress and geometric imperfections influence the collapse behavior. Additionally, validity and limitations of the adopted modeling approach is discussed. Since the study is limited to a local model comprising only a few stiffener bays, the discussion focused on local collapse behavior rather than the global response of the full pressure hull and any end bay effects at stiff bulkheads.

6.1 Influence of individual residual stress sources on collapse pressure

The parametric study presented that the influence of individual residual stress sources on collapse pressure depends strongly on both location of the stress field and the stress component involved. Among the investigated cases, cold bending, the plating-web fillet weld and girth weld were identified as the sources producing the clearest reduction in collapse pressure, whereas the web-flange fillet weld and seam weld had only a minor influence within the investigated range.

For the cold bent plating and flanges, the collapse pressure decreased noticeably with increasing amplitude, x, of the stress profiles. As illustrated in Figure 5.3, increasing x amplifies the peak stress magnitude towards the yield stress. The corresponding pressure-displacement curves show that increasing x causes an earlier deviation from the reference response and a more rapid reduction in stiffness. As the structure is subjected to increasing external hydrostatic pressure, the hull experiences compressive stresses in both the axial and hoop directions. This effectively shifts the through-thickness stress profiles toward the compressive side. Once the effective stress at a given point reaches the yield stress, that region can no longer carry additional stress due to the adopted ideally plastic material model, and the load must be redistributed to the surrounding material that remains elastic. This loss in load capacity represents the change in tangent stiffness in the pressure-displacement curves, and the first region that yields is the compressive peak. Thus, the observed reduction in collapse pressure from the cold bending cases is consistent with the fact that the residual stress field places parts of the thickness in a pre-compressed state and thus closer to yielding than in the ideal, stress-free structure.

When examining the axial stress response for all cases, the relaxed axial stress profile generally becomes either self-equilibrating or dominated by bending stress. This is particularly clear for the plating-web fillet weld when the membrane stress is varied, where the relaxed axial stress profile becomes nearly identical despite different initially applied membrane stress levels. Table 5.3 also shows that the axial shrinkage, δv, for the plating-web fillet weld increases with increasing membrane stress, while remaining approximately constant when bending stress is varied. This suggests that a significant part of the initially applied membrane stress is released through axial contraction of the hull, since neither the structure nor the boundary conditions provide strong resistance against this deformation. Since welding induces contraction during cooling, the observed axial shrinkage is consistent with the behavior expected from the plating-web fillet weld configuration.

The remaining axial bending stress in the relaxed profiles can also be interpreted in relation to the structural arrangement of the hull. For the plating-web fillet weld, the welds on the two sides of the web introduce opposing contributions, which largely balance each other and therefore do not primarily cause the ring stiffener to tilt during relaxation. Instead, the ring stiffener is kept approximately upright, while some radial deformation of the stiffener-plating region may still develop. The plating between two adjacent stiffeners, on the other hand, is subjected to opposing moments that bend the midbay inward.

The hoop stress in the plating-web fillet weld exhibits a slightly different behavior. Figure 5.6 shows that the hoop stress only relaxes partially, regardless of the magnitude of the varied membrane or bending stress. When the initial stress is applied, the entire weld region is placed in tension while the surrounding material is stress free. During relaxation, the tensile residual stress is reduced, and the surrounding region develops compressive stress, together forming a local equilibrium. The reduction in tensile hoop membrane stress is therefore associated with an increase of compressive hoop stress in the adjacent ring stiffeners and plating outside of the weld region.

An increasing compressive hoop stress at midbay can also be observed when varying both membrane and bending stress for the plating-web fillet weld. For the membrane variation, $w_{\max}$ from Table 5.3 as well as the radial displacement contours in Appendix A2 show that even though δw remains nearly constant with increasing membrane stress, the entire structure becomes more radially compressed as the membrane stresses increases. This provides a source for the increased compressive hoop stress at midbay. For the bending variation, the membrane stress is kept constant. The corresponding $w_{\max}$ and contour plots in Appendix A2 show a smaller change in total radial deformation. Table 5.3 shows however an increase in inward radial deformation at midbay, δw, which also contributes to compressive hoop stress.

The girth weld showed a different behavior, where both the membrane component and the sign of the bending component influenced the collapse response, indicating that not only the stress magnitude but also the direction of the induced deformation is important. For the membrane variation, the girth weld produced a clear reduction in collapse pressure. This can be related to the location of the weld in the hull. Since the girth weld extends around the circumference of the shell in the stiffener bay, 1/3 of the stiffener spacing away from one stiffener, the tensile stress in the weld will put the surrounding material in compression, as in the case with plating-web fillet weld. However, the location of the weld, compared to the plating-web fillet weld, has less stiffness as it is in the bay rather than directly connected to a ring stiffener. This is reflected by the increase in $w_{\max}$, which shows that the membrane component leads to a larger overall radial contraction after relaxation.

The bending component of the girth weld showed a strong dependence on its sign. Outward bending had only a limited influence, but an increase in collapse pressure. This can be interpreted as a partial counteraction of the inward deformation tendency of the shell under external pressure. By bending the shell outward in the relaxed state, the weld introduces a deformation that opposes the collapse-related inward radial motion, thereby reducing the severity of the response. This behavior can be compared to designing the DV groove in a way that introduces an outward bending stress which acts as a partially favorable imperfection which improves the impact from the weld despite its pliant location.

Inward bending on the other hand showed the opposite trend compared to outward bending. The inward bending component produced larger radial deformation in the relaxed state, and an earlier deviation from the reference pressure-displacement response. This suggests that inward bending introduces a deformation pattern aligned with the collapse mode. In addition to the increased deformation, the associated stress redistribution also becomes more unfavorable, since the shell is driven further into a stress state compatible with pressure-induced collapse. The inward bending case is therefore destructive, both because it increases the initial deformation and because it contributes to a more critical stress state prior to loading.

6.2 Combined effect of residual stresses on structural capacity

In the study with combined residual stresses, all residual stresses considered in the parametric study are applied simultaneously to quantify their combined effect on the collapse pressure. The outward bending configuration of the girth weld was adopted in the combined study, since the parametric study indicated that it was less detrimental to collapse resistance than inward bending.

The results show that the combined residual stress field leads to a clear reduction in collapse pressure for all investigated cases. For the cases with L_c = 450 mm, the HY100 case exhibits a higher collapse pressure (6.94 MPa) than the HY80 case (6.04 MPa), which is expected due to the higher yield stress of HY100 and that the higher-strength materials can withstand greater external pressure before yielding initiates. At the same time, the relative reduction in collapse pressure is greater for HY100 (14.6%) than HY80 (11.0%). This is consistent with the modeling choice of scaling the initial residual stresses relative to the yield stress in accordance to BS 7910, meaning that larger residual stresses were introduced in the HY100 case, thereby reducing the collapse pressure to a greater extent. This indicates that the residual stresses becomes more influential for pressure hulls made of steels with higher yield strength.

Case 2, with a larger stiffener spacing of L_c = 600 mm and HY80 steel, exhibits lower collapse pressures for both the plastic reference and the residual stress analysis (5.83 MPa and 5.22 MPa, respectively) than for the case with L_c = 450 mm. This demonstrates that stiffener spacing has a great influence on structural collapse resistance. However, the relative reduction in collapse pressure for case 2 remains close to that of case 1 (10.5% and 11.0%, respectively). The relaxed radial deformation in Bay 2 is nearly identical for the two HY80 cases, as observed in Table 5.6, which suggests that the relaxed midbay stress states are similar despite the different stiffener spacing. This may explain why the relative reduction caused by the combined residual stress field is of comparable magnitude in the two cases, even though the absolute collapse pressures differ.

Comparing the parametric study with the combined residual stress case, it is clear that the simultaneous application of all residual stress sources leads to a greater reduction in collapse pressure than considering individual contributions separately. A direct comparison with the most severe parametric case must, however, be made with care. From the parametric study, in Figure 5.2, the largest reduction of approximately 10.0% was obtained from the girth weld, varying the membrane component at a residual stress magnitude equal to the yield stress. In the combined study, by contrast, the residual stress magnitude was calibrated to obtain relaxed stress distributions similar to BS 7910. The applied parameters listed in Table 4.6 vary between stress components, with some below and some above unity, so comparisons should therefore be made at corresponding multiplier levels in the parametric study.

Even with these calibrated stress levels, the combined residual stress analysis for case 1 showed a reduction in collapse pressure of 11.0%. This indicates that the combined effect of several manufacturing-induced residual stress sources is more detrimental than the isolated effect of any single contribution alone. A possible explanation is that several of the included residual stress fields introduce compressive stresses in the midbay region, where the structure is the most vulnerable for the studied geometry. When applied simultaneously, these stress contributions add up to a larger preload in the plating and are also associated with a larger overall deformation. The combined residual stress state therefore becomes more harmful than the individual stress sources. For structural assessment, the combined residual stress state is therefore more relevant than any single individual stress source alone.

6.3 Comparison of residual stress and geometric imperfection effects on collapse pressure

Next, the influence on collapse pressure of combined residual stresses compared to geometric imperfections resulting from the relaxed stress state is discussed.

Comparing the cases separately for the combined residual stresses and geometric imperfections gives 11.0% to 6.8%, 10.5% to 5.0% and 14.6% to 5.3%, for each case. It is thus evident that residual stresses and their related geometric imperfections have a more pronounced effect on collapse pressure than the geometric imperfection from the relaxed stress state alone. This is likely due to initial compressive stresses, which are present in the combined residual stress cases but non-present in the geometric imperfect cases. This means that the analyses with combined residual stresses are already subjected to compressive stresses before the external pressure loading is applied. These initial compressive stresses promoting earlier yielding and loss in stiffness. Although tensile residual stresses are also present and may locally increase the stiffness, the overall effect of the residual stress field is a reduction in collapse pressure.

In contrast, the imperfect analyses are not initially pre-stressed. The geometric imperfections are introduced only through the relaxed deformation shape, without any additional residual stress fields. Consequently, these cases do not experience initial compressive stresses prior to external loading, which explains why their collapse pressures remain higher than those of the residual stress analyses. This is also reflected in the von Mises contour plots for the imperfect cases, which appear more similar to each other than the corresponding residual stress analyses. Since the imperfect cases differ only by material and geometry, the distribution of stresses generated from external loading remains generally similar. Furthermore, the contour plots are scaled with respect to the respective yield stress resulting in similar appearances but different stress levels. For all cases, the largest compressive stresses occur in the midbay region. For Case 1 and 2, the entire cross-section at midbay has yielded as observed in the von Mises stress plots for the residual stress case, see Figure 5.12 b) and Figure 5.13 b). However, for case 3, Figure 5.14 b), partial through-thickness yielding has occurred, while the corresponding pressure-displacement plot indicates that the structure has collapsed.

To consult similar work in this field, the publications done by Franquetto and Neto [3] and Kendrick [5] are recalled. In the paper by Franquetto and Neto [3], the effect of manufacturing-induced residual stresses combined with geometric imperfections on collapse pressure is investigated. In that study, geometric imperfections are prescribed and varied according to analytical expressions representing out-of-roundness and out-of-straightness defects. This showed how the significance of residual stress was reduced as geometric imperfections were amplified. The imperfections are therefore not obtained from a relaxed stress state, as in this study. Instead, Franquetto and Neto [3] introduce initial residual stress fields onto already imperfect hull geometries and subsequently performs nonlinear collapse analyses. The study therefore considers a range of assumed geometric defect scenarios and evaluates how these interact with residual stresses. Kendrick [5] also mentions briefly how the effect of residual stress reduces with increased geometric imperfections. In contrast, the present study investigates geometric imperfections that naturally arise from the relaxed stress state after combined residual stresses have been applied. Consequently, the residual stresses and geometric imperfections are mechanically linked, since the imperfections develop as a result of stress redistribution.

As discussed previously, geometric imperfections are unavoidable in manufacturing processes. The present study specifically examined the imperfections induced by the applied residual stresses. However, geometric imperfections may also originate from other manufacturing processes, such as fitting. For example, if two shell sections are misaligned prior to welding, out-of-straightness imperfections already exist. Subsequent welding may then further amplify or modify these imperfections, possibly in a manner similar to the one shown in this work.

6.4 Validity and limitations of the modeling approach

The modeling approach adopted in this thesis provides a consistent framework for evaluating the influence of residual stresses and geometric imperfections on the collapse behavior of a ring stiffened pressure hull segment. At the same time, several limitations should be recognized when interpreting the results.

A first limitation concerns the residual stress profiles adopted from BS 7910. The standard appears to have been developed primarily for pipelines, which differ from submarine pressure hulls. In addition, it is not clear whether the measurements were obtained from structures that had been cold bent prior to welding, nor exactly where in the welded joint the measurement was taken. However, the weld types adopted in this work are of the same general type as those considered in the standard, and the employed materials and geometry fall within the assessment ranges described in BS 7910. The adopted profiles should therefore be regarded as conservative approximations rather than exact representations of the manufactured structure.

A second limitation concerns the definition of weld width. In this thesis, the weld was represented by an assumed affected region over which the residual stresses were prescribed. This width was not intended to represent the physical fusion zone alone, but rather the region significantly affected by welding. In reality, the magnitude of the residual stress field would vary gradually with the distance from the weld rather than change abruptly at the edge of the element set. Such a gradual spatial variation is discussed, for example, by Dong et al. [13] and Ma et al. [14], where the residual stress field is described as a function of distance from the weld toe. This, together with the large number of parameters on which welding residual stresses depend, motivated the simplified modeling choice adopted in the present work. The weld width study should therefore be interpreted as a sensitivity study of the assumed weld-affected region rather than a direct representation of the true weld and HAZ geometry.

The combined residual stress study introduces a further source of uncertainty. Since the profiles from BS 7910 represent relaxed residual stress states, the combined field used in the finite element model had to be calibrated to obtain a similar relaxed distribution after equilibration. This calibration was performed by scaling stress magnitudes in the different weld regions using multipliers of the yield stress. A different calibration strategy, such as one based on inherent strain or a detailed thermo-mechanical welding simulation might have produced a different relaxed stress field. The combined stress state should therefore be viewed as a calibrated representation rather than a uniquely determined residual stress field.

Another limitation is that not all potentially relevant residual stress fields were modeled in equal detail. In particular, neither seam weld residual stresses in the web and flange nor tension stresses in the web related to the fillet welds were represented. This was a deliberate simplification. Nevertheless, it means that the total residual stress state in the actual structure is only partially represented, and some local effects may therefore have been excluded.

Despite the limitations, the modeling approach is considered sufficiently robust for the purpose of the thesis. The main value of the study lies in the possibility to identify mechanisms and clarify the relative influence of different manufacturing-induced effects on collapse behavior. By contrast, the absolute values of the calculated collapse pressures should be interpreted with more caution, since they depend on simplified residual stress definitions, assumed weld-affected widths, and the adopted calibration procedure.

7 Conclusion

The influence of residual stresses and geometric imperfections on the collapse behavior of a ring stiffened submarine pressure hull subjected to external pressure has been studied using nonlinear finite element analyses on local pressure hull segments intended to capture the local response away from bulkheads. The focus was on individual residual stress sources, the combined effect of several residual stress fields, and the effect of geometric imperfections derived from the relaxed deformation state.

The influence of individual residual stress sources was found to depend strongly on both the location of the stress field and the stress component involved. Cold bending, the plating-web fillet weld, and the girth weld were identified as the most influential sources, whereas the web-flange fillet weld and seam weld only had a minor effect.

Residual stresses were found to influence collapse behavior through two mechanisms: the deformation they induce and the accompanying redistribution of stresses throughout the hull. Residual stresses were found to be the most harmful when they introduce compressive stresses in structurally vulnerable regions of the pressure hull, which in the present work was in the shell plating between ring stiffeners. Under external pressure, such regions reach yielding at a lower applied pressure when an initial compressive residual stress is present. Therefore, the cold bent plating, plating-web fillet welds and girth welds were identified as particularly detrimental. In addition, the sign of the induced deformation was found to be important. Stress fields that introduce inward radial deformation, aligned with the collapse deformation, increase the severity of the response, whereas outward radial deformation may partially counteract this tendency. The most harmful cases are therefore those where both effects act in the same unfavorable direction.

With respect to the objectives of quantifying the combined effect of residual stresses on structural capacity and comparing this effect with that of geometric imperfections, the results showed that both residual stresses and geometric imperfections reduce collapse pressure, but that the combined residual stress field had a stronger influence. When residual stress contributions from all considered sources (cold bending, fillet welds, girth welds, and seam welds) were applied simultaneously, collapse pressure was reduced by 10.5 – 14.6% for the investigated cases relative to the corresponding ideal reference analyses. The geometric imperfections obtained from the residual stresses of the combined case also reduced the collapse pressure, but to a smaller extent, 5.0 – 6.8% for the corresponding cases.

Although the study is based on simplified residual stress definitions, calibrated combined stress fields, and local pressure hull models, the framework provides a consistent basis for comparing the relative influence of different manufacturing-induced effects. The main contribution of this work is therefore not an exact prediction of collapse pressure for a specific manufactured submarine hull, but rather an improved understanding of how different manufacturing-induced residual stress sources influence collapse behavior and how these effects interact with geometric imperfections.

References

[1] I. M. Robertson, "Analytical Calculations of Fatigue Loading of Submarine Hulls," 1990.

[2] D. Faulkner, "Effects of residual stresses on the ductile strength of plane welded grillages and of ring stiffened cylinders," Journal of Strain Analysis for Engineering Design, 1977.

[3] P. Franquetto and M. Neto, "Experimental Residual Stress and Geometric Imperfections on Pressure Hull Instability Analysis," *Journal of Offshore Mechanics and Arctic Engineering,* vol. 140, no. 3, p. 031401, 2018.

[4] X. Fiquet, "Measurement of Bending Residual Stress on a Hull Section of a Submarine," *Conference: ASME 2012 31st International Conference on Ocean, Offshore and Arctic Engineering,* July 2012.

[5] S. Kendrick, Ring-stiffened cylinders under external pressure (Chapter 3 from Shell structures - Stability and Strength R. Narayanan), Elsevier, 1985.

[6] C. T. F. Ross, Pressure vessels under external pressure, 1990.

[7] J. MacKay, F. van Keulen and M. J. Smith, "Quantifying the accuracy of numerical collapse predictions for the design of submarine pressure hulls," *Thin-Walled Structures,* vol. 49, no. 1, p. 145–156, 2011.

[8] J. M. Rotter, "Cylindrical shells under axial compression," in *Buckling of Thin Metal Structures*, 2003.

[9] M. Ristinmaa and C. Ljung, "An introduction to Stability Analysis," *Lund University, Division of Solid Mechanics,* 2002.

[10] M. Ristinmaa and N. S. Ottosen, "The Mechanics of Contitutive Modelling," *Lund University, Division of Solid Mechanics,* 2005.

[11] B. S. Bedenik and C. B. Besant, "Analysis of Engineering Structures," Woodhead Publishing Series in Civil and Structural Engineering, 1999, pp. 308-320.

[12] P. J. Withers, "Residual stress and its role in failure," *Reports on Progress in Physics,* vol. 70, pp. 2211-2264, 2007.

[13] P. Dong, S. Song and X. Pei, "An IIW residual stress profile estimation scheme for girth welds in pressure vessel and piping components," *Weld World,* 2015.

[14] N. Ma, D. Deng, N. Osawa, S. Rashed and H. Murakawa, Welding Deformation and Residual Stress Prevention, Butterworth-Heinemann, 2022.

[15] British Standards Institution, "BS 7910: Guide to mehthods for assessing the acceptability of flaws in metallic structures," 2005.

[16] J. J. Reijmers, M. Kaminski and D. Stapersma, "Analytical formulations and comparison of collapse models for risk analysis of axisymmetrically imperfect ring-stiffened cylinders under hydrostatic pressure," *Marine Structures ,* vol. 83, no. 203161, 2022.

[17] J. Semple, D. Bechetti, W. Zhang, J. E. Norkett and C. R. Fisher, "Temperature-Dependent Material Property Databases for Marine Steels - Part 5: HY-80," 2023.

[18] A. Ishigami, M. J. Roy, J. N. Walsh and P. J. Withers, "The effect of the weld fusion zone shape on residual stress in submerged arc welding," *International Journal of Advanced Manufacturing Technology,* vol. 90, pp. 3451-3464, 2017.

Appendix A – Parametric study

This appendix presents the detailed results from the parametric study of the individual residual stress sources. For each case, tabulated collapse pressures and deformation measures are shown together with the applied through-thickness residual stress profiles, the corresponding pressure-displacement responses, and the relaxed deformation fields. The appendix is intended to complement the summary presented in Figure 5.2 and to illustrate how the individual residual stress sources influence collapse behavior and relaxation response in more detail.

A1 – Cold bending

The results for cold bending of both the plating and flange show a clear reduction in collapse pressure with increasing stress amplitude, shown in Table A.1. The through-thickness stress profile retains its self-equilibrating Z-shape during relaxation for both cases, while the increasing amplitude moves the compressive peak closer to the yield stress, shown in Figure A.1. This leads to earlier yielding under external pressure and a more pronounced reduction in structural stiffness, which is reflected in the pressure-displacement curves in Figure A.2. The effect is stronger for the cold bent plating compared to the flange, indicating that residual stress in the plating is more detrimental than in the flange.

Table A.1: Results for the cold bent plating and flange cases, including multiplier of the maximum stress relative to the yield stress, collapse pressure, and change in collapse pressure relative to the ideal, stress-free reference analysis.

Cold bending of	**Multiplier *x*:**	**0.0**	**0.4**	**0.6**	**0.8**	**1.0**
Plating	Collapse pressure p_c [MPa]	6.80	6.61	6.54	6.46	6.36
	Change from reference (%)	0.0	-2.8	-3.8	-5.0	-6.5
Flange	Collapse pressure p_c [MPa]	6.80	6.73	6.61	6.56	6.31
	Change from reference (%)	0.0	-1.0	-2.8	-3.5	-7.2

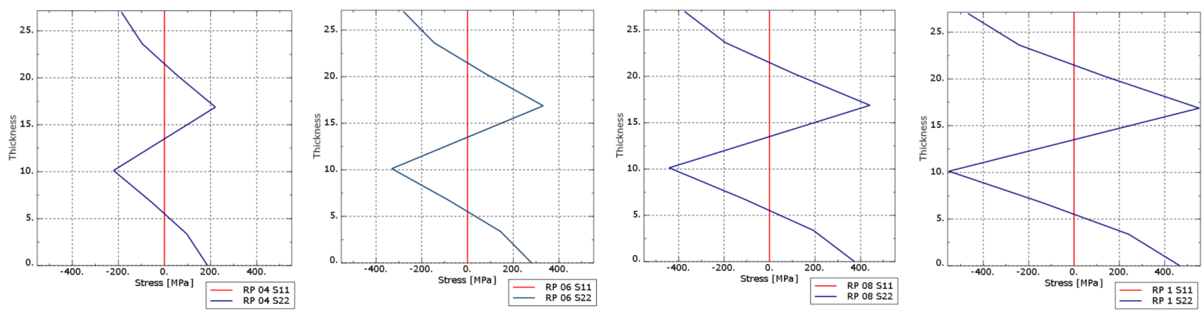

a) $x = 0.4$ b) $x = 0.6$ c) $x = 0.8$ d) $x = 1.0$

Figure A.1: Through-thickness residual stress profiles for the cold-cold bent plating for the investigated stress levels. The horizontal axis shows the normalized thickness coordinate, and the vertical axis shows the residual stress normalized by the yield stress.

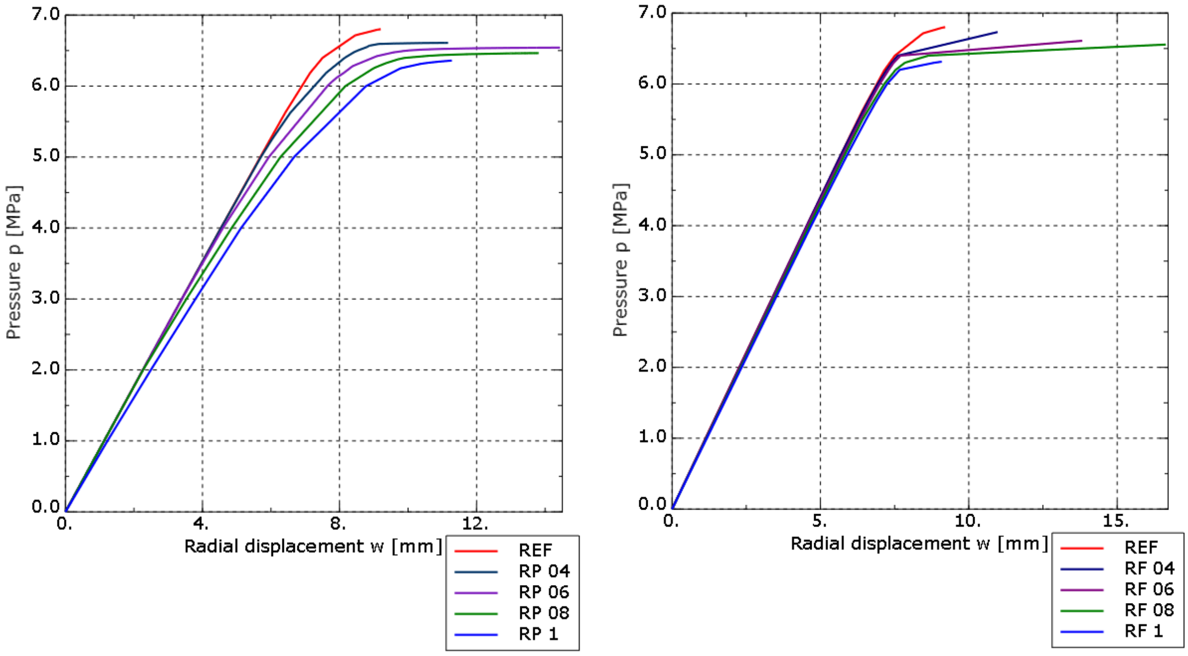

a) Cold bent plating

b) Cold bent flange

Figure A.2: Pressure-displacement response for the cold-cold bent plating and flange for the investigated stress levels.

A2 - Plating-web fillet weld

Table A.2 present the results for the plating-web fillet weld with varied membrane and bending stress. The response from increasing the membrane stress component is shown in Figure A.3-Figure A.5 and Figure A.7 a). Increasing the membrane component leads to a clear reduction in collapse pressure. The relaxed stress profiles show that the initially applied stress distribution changes during the relaxation step, while the contour plots show increasing deformation in the shell region around the weld. The pressure-displacement curves also deviate progressively from the reference response as the membrane stress is increased.

Figure A.5, Figure A.6 and Figure A.7 b) present the results for the plating-web fillet weld with varied bending stress. The collapse pressure decreases as the bending component is increased, and the relaxed deformation becomes more pronounced. Compared with the membrane variation, the bending variation gives a similar overall trend, with increasing deviation from the reference pressure-displacement response as the stress level increases. The relaxed contour plots show that the deformation is concentrated in the shell region between the stiffeners, giving a slight outward deformation near the stiffeners and a larger inward deformation midbay.

Table A.2: Results for the plating-web fillet weld with varied membrane stress, including collapse pressure, change in collapse pressure relative to the ideal, stress-free reference analysis, maximum radial displacement after relaxation w_{max}, and measured bay deformations δ_w and δ_v.

Varied parameter	**Multiplier x**	**0.0**	**0.4**	**0.6**	**0.8**	**1.0**
Membrane	Collapse pressure p_c [MPa]	6.80	6.52	6.49	6.43	6.39
	Change from reference (%)	0.0	-4.1	-4.6	-5.4	-6.1
	w_{max} [mm]	0.0	-0.58	-0.73	-0.87	-1.01
	δw [mm]	0.0	0.36	0.35	0.33	0.32
	δv [mm]	0.0	0.15	0.23	0.32	0.40
Bending	Collapse pressure p_c [MPa]	6.80	6.55	6.49	6.40	6.28
	Change from reference (%)	0.0	-3.7	-4.6	-6.0	-7.7
	w_{max} [mm]	0.0	-0.50	-0.60	-0.71	-0.82
	δw [mm]	0.0	0.28	0.44	0.59	0.75
	δv [mm]	0.0	0.20	0.20	0.20	0.20

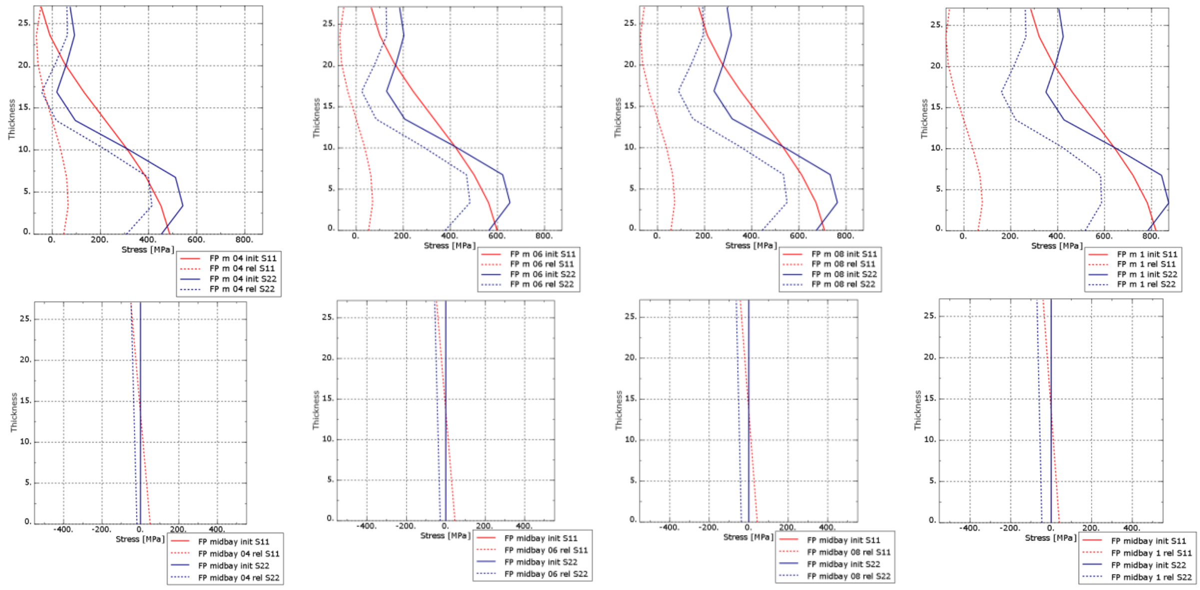

a) $x = 0.4$ b) $x = 0.6$ c) $x = 0.8$ d) $x = 1.0$

Figure A.3: Through-thickness residual stress profiles for the varied membrane stress in the plating-web fillet weld and the corresponding midbay response. The vertical axis shows the thickness of the material, where 0 corresponds to the inside surface of the plating. The horizontal axis shows stress. The initial stress is shown as a solid line and the relaxed profile as a dashed line. Red indicates axial stress $(S11)$ and blue indicates hoop stress $(S22)$.

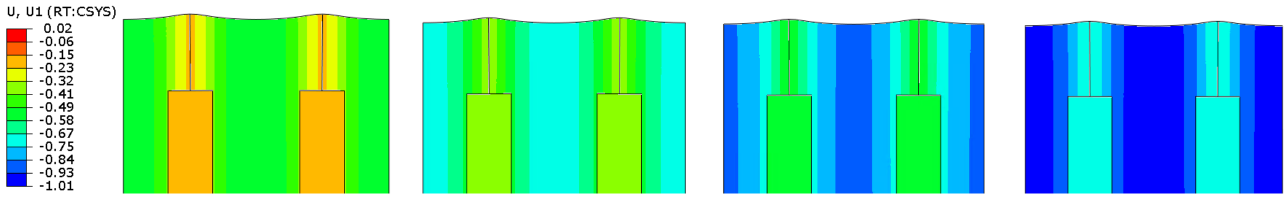

a) $x = 0.4$ b) $x = 0.6$ c) $x = 0.8$ d) $x = 1.0$

Figure A.4: Radial displacement after relaxation for the plating-web fillet weld with varied membrane stress. Units are shown in mm and the deformation is scaled 25 times.

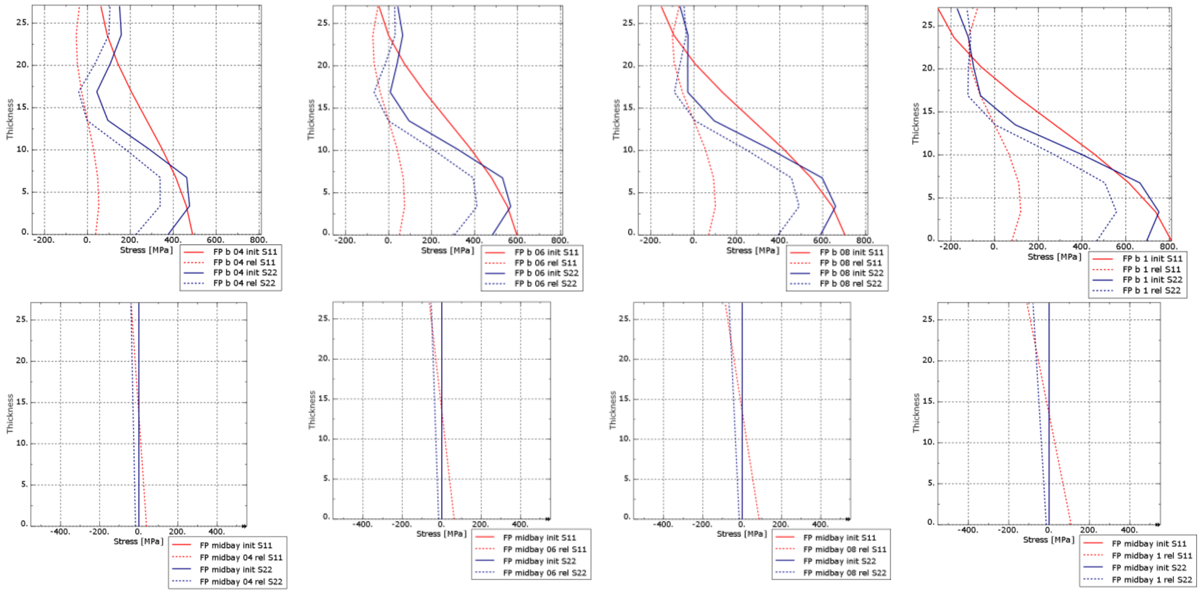

a) $x = 0.4$ b) $x = 0.6$ c) $x = 0.8$ d) $x = 1.0$

Figure A.5: Through-thickness residual stress profiles for the varied bending stress in the plating-web fillet weld and the corresponding midbay response. The vertical axis shows the thickness of the material, where 0 corresponds to the inside surface of the plating. The horizontal axis shows stress. The initial stress is shown as a solid line and the relaxed profile as a dashed line. Red indicates axial stress $(S11)$and blue indicates hoop stress $(S22)$.

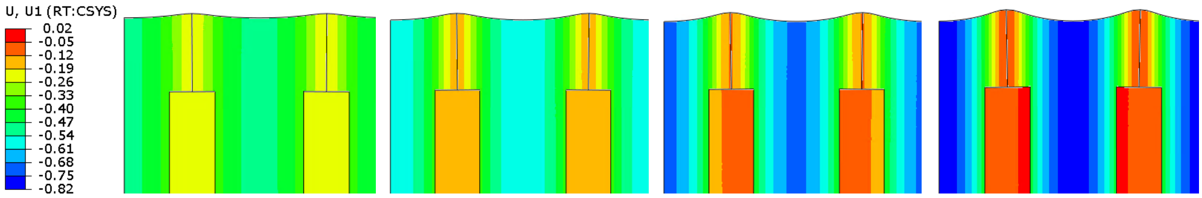

a) $x = 0.4$ b) $x = 0.6$ c) $x = 0.8$ d) $x = 1.0$

Figure A.6: Radial displacement after relaxation for the plating-web fillet weld with varied bending stress. Units are shown in mm and the deformation is scaled 25 times.

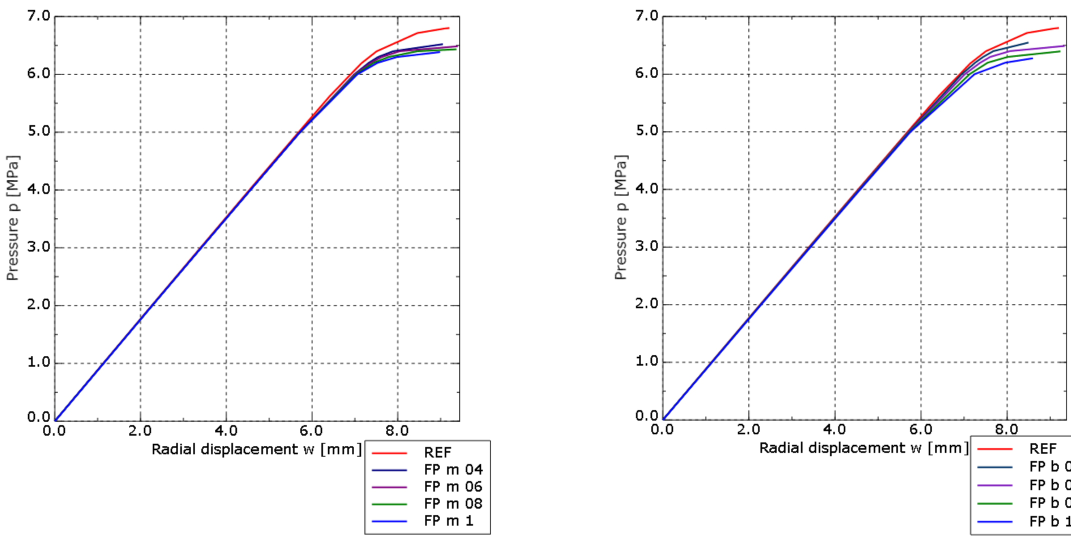

a) Pressure-displacement plot for varied membrane stress in the plating-web fillet weld

b) Pressure-displacement plot for varied bending stress in the plating-web fillet weld

Figure A.7: Pressure-displacement response for the plating-web fillet weld with varied membrane and bending stress.

A3 - Web-flange fillet weld

Table A.3 present the results for the web-flange fillet weld with varied membrane and bending stress. The through-thickness plots in Figure A.8 show that the initial stress profiles from varying the membrane stress component reduce during relaxation. The axial stress relaxes to the same profile, about 0, while the hoop stress only reduces partially. The response at the edge of the flange is only affected in the circumferential direction. The pressure-displacement curves for the varied membrane stress component in the web-flange fillet weld, seen in Figure A.10 a), remains close to the reference response for all investigated levels.

Figure A.9 show the initial and relaxed through-thickness stress profiles in the web-flange fillet weld when varying the bending stress. Just like when varying the membrane stress, the axial stress relaxes to near zero and the hoops stress only relaxes partially, with only hoop membrane stress as a response at the edge of the flange. The pressure-displacement plot shows some differences between the different magnitudes, but similar collapse pressures.

Table A.3: Results for the web-flange fillet weld with varied membrane stress, including collapse pressure, change in collapse pressure relative to the ideal, stress-free reference analysis, maximum radial displacement after relaxation w_{max}, and measured bay deformations $\delta_w$and δ_v.

Varied parameter	**Multiplier x**	**0.0**	**0.4**	**0.6**	**0.8**	**1.0**
Membrane	Collapse pressure p_c [MPa]	6.80	6.67	6.66	6.61	6.60
	Change from reference (%)	0.0	-2.0	-2.0	-2.8	-2.9
	$w_{\max}$ [mm]	0.0	0.32	0.45	0.58	0.70
	δw [mm]	0.0	0.036	0.050	0.067	0.079
	δv [mm]	0.0	0.022	0.031	0.040	0.048
Bending	Collapse pressure p_c [MPa]	6.80	6.66	6.66	6.65	6.64
	Change from reference (%)	0.0	-2.0	-2.0	-2.2	-2.4
	$w_{\max}$ [mm]	0.0	0.28	0.29	0.30	0.30
	δw [mm]	0.0	0.032	0.033	0.034	0.035
	δv [mm]	0.0	0.019	0.020	0.020	0.021

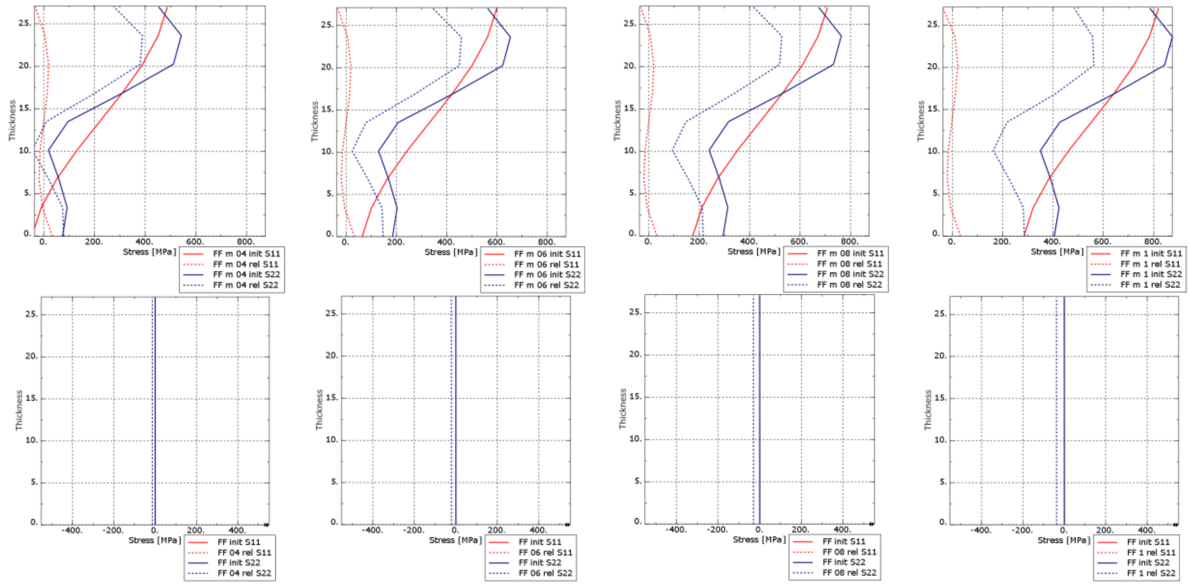

a) $x = 0.4$ b) $x = 0.6$ c) $x = 0.8$ d) $x = 1.0$

Figure A.8: Through-thickness residual stress profiles for the varied membrane stress in the web-flange fillet weld and the corresponding response at the end of the flange. The vertical axis shows the thickness of the material, where 0 corresponds to the inside surface of the plating. The horizontal axis shows stress. The initial stress is shown as a solid line and the relaxed profile as a dashed line. Red indicates axial stress ($S11$)and blue indicates hoop stress ($S22$).

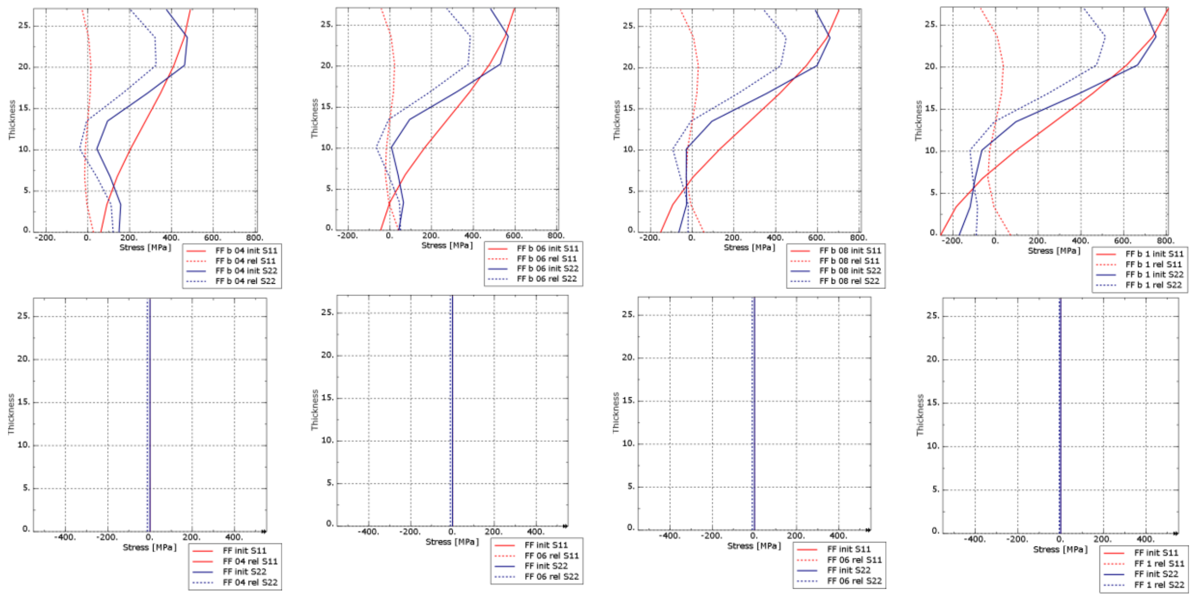

a) $x = 0.4$ b) $x = 0.6$ c) $x = 0.8$ d) $x = 1.0$

Figure A.9: Through-thickness residual stress profiles for the varied bending stress in the web-flange fillet weld and the corresponding response at the edge of the flange. The vertical axis shows the thickness of the material, where 0 corresponds to the inside surface of the plating. The horizontal axis shows stress. The initial stress is shown as a solid line and the relaxed profile as a dashed line. Red indicates axial stress ($S11$)and blue indicates hoop stress ($S22$).

.

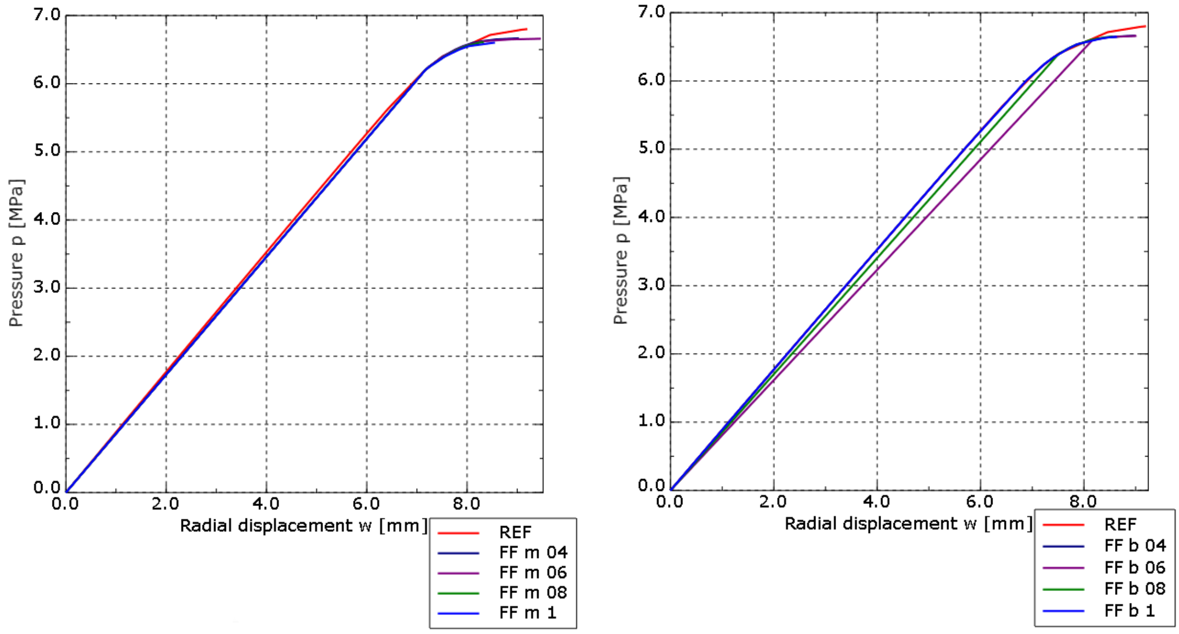

a) Pressure-displacement plot for varied membrane stress in the web-flange fillet weld

b) Pressure-displacement plot for varied bending stress in the web-flange fillet weld

Figure A.10: Pressure-displacement response for the web-flange fillet weld with varied membrane and bending stress.

A4 - Girth weld

Table A.4 present the results for the girth weld with varied membrane stress and both outward and inward bending stress. Varying membrane stress and the inward bending stress has the highest effect on collapse pressure while the inward bending shows the largest maximum radial deformation w_{max} in the relaxed state. The response form increasing the membrane stress is shown in Figure A.11 - Figure A.12 and Figure A.17 a). Increasing the membrane component leads to a clear reduction in collapse pressure and a progressively larger deviation from the reference pressure-displacement response. The relaxed contour plots show increasing radial deformation in the weld region as the stress level is increased.

The response form increasing the outward bending stress is shown in Figure A.13 - Figure A.14 and Figure A.17 b). In this case, the pressure-displacement curves show small differences between the different magnitudes of bending stress with a slight increase in collapse pressure as the outward bending stress increases, but an overall decrease from the ideal reference collapse pressure. The contour plots show an increased peak outward in the girth weld as the outward bending is increased, resulting in a straighter hull and counteracts the otherwise radial shrinkage of welds.

The response from increasing the inward bending stress, shown in Figure A.15, Figure A.16 and Figure A.17 c), shows the opposite effect to the outward bending stress. The contour plots show increasing radial deformation in the bay with the girth weld and the pressure-displacement curves show a similar but decreasing response as the inward bending stress is increased.

Table A.4: Results for the girth weld with varied membrane and bending (inward and outward) stress, including collapse pressure, change in collapse pressure relative to the ideal, stress-free reference analysis, maximum radial displacement after relaxation w_{max}, and measured bay deformations $\delta_w$and δ_v.

Varied parameter	**Multiplier x**	**Ref**	**0.4**	**0.6**	**0.8**	**1.0**
Membrane	Collapse pressure p_c [MPa]	6.80	6.58	6.53	6.41	6.05
	Change from reference (%)	0.0	-3.2	-3.9	-5.8	-11
	$w_{\max}$ [mm]	0.0	0.11	0.19	0.28	0.38
	δw [mm]	0.0	-0.029	0.050	0.093	0.14
	δv [mm]	0.0	0.054	0.075	0.096	0.12
Outward bending	Collapse pressure p_c [MPa]	6.80	6.44	6.46	6.47	6.49
	Change from reference (%)	0.0	-5.3	-5.0	-4.9	-4.6
	$w_{\max}$ [mm]	0.0	0.32	0.27	0.24	0.26
	δw [mm]	0.0	0.063	-0.055	-0.18	-0.30
	δv [mm]	0.0	0.034	0.035	0.035	0.036
Inward bending	Collapse pressure p_c [MPa]	6.80	6.40	6.38	6.37	6.33
	Change from reference (%)	0.0	-5.9	-6.2	-6.4	-6.9
	$w_{\max}$ [mm]	0.0	0.64	0.75	0.86	0.96
	δw [mm]	0.0	0.42	0.53	0.64	0.75
	δv [mm]	0.0	0.034	0.034	0.034	0.034

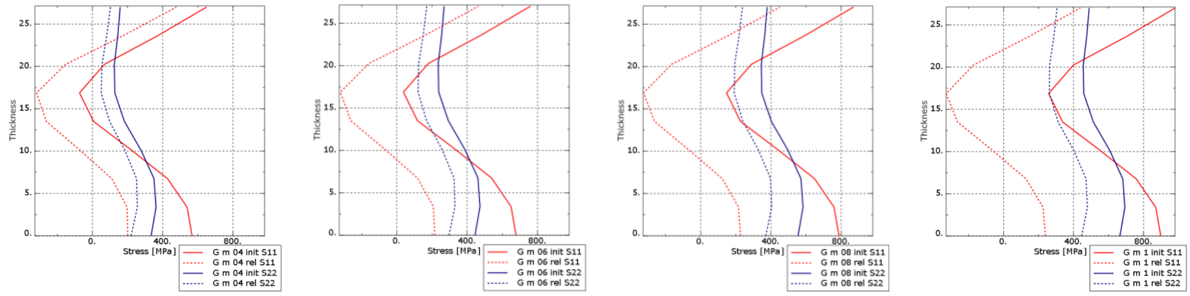

a) $x = 0.4$ b) $x = 0.6$ c) $x = 0.8$ d) $x = 1.0$

Figure A.11: Through-thickness residual stress profiles for the varied membrane stress in the girth weld. The vertical axis shows the thickness of the material, where 0 corresponds to the inside surface of the plating. The horizontal axis shows stress. The initial stress is shown as a solid line and the relaxed profile as a dashed line. Red indicates axial stress $(S11)$and blue indicates hoop stress $(S22)$.

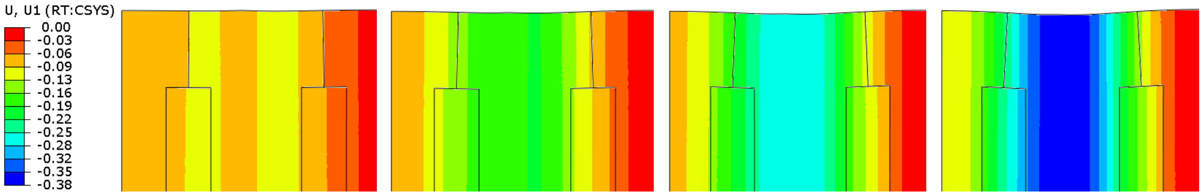

a) $x = 0.4$ b) $x = 0.6$ c) $x = 0.8$ d) $x = 1.0$

Figure A.12: Radial displacement after relaxation for the plating-web fillet weld with varied membrane stress. Units are shown in mm and the deformation is scaled 25 times.

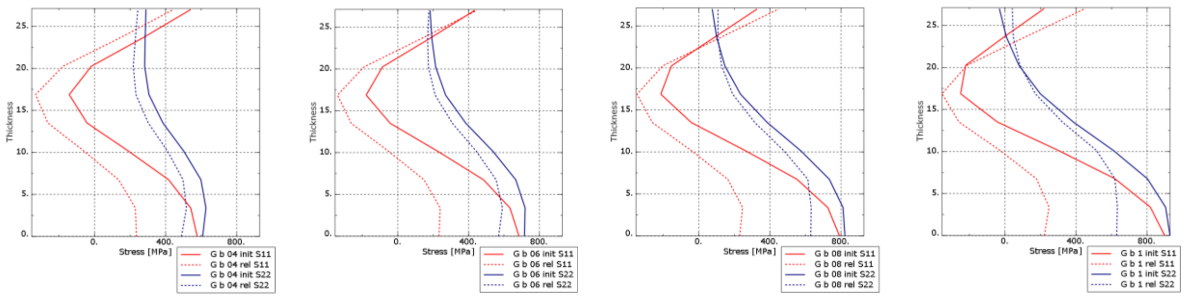

a) $x = 0.4$ b) $x = 0.6$ c) $x = 0.8$ d) $x = 1.0$

Figure A.13: Through-thickness residual stress profiles for the varied outward bending stress in the girth weld. The vertical axis shows the thickness of the material, where 0 corresponds to the inside surface of the plating. The horizontal axis shows stress. The initial stress is shown as a solid line and the relaxed profile as a dashed line. Red indicates axial stress $(S11)$and blue indicates hoop stress $(S22)$.

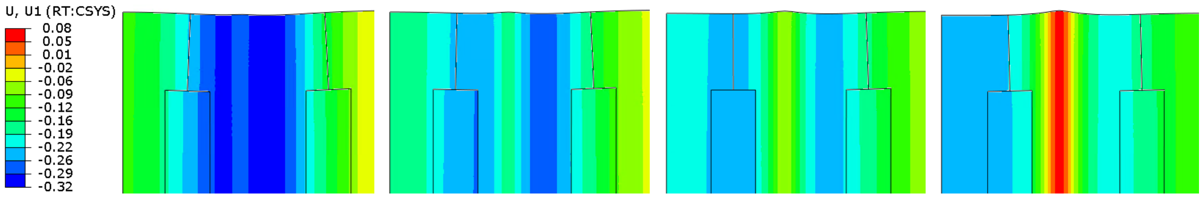

a) $x = 0.4$ b) $x = 0.6$ c) $x = 0.8$ d) $x = 1.0$

Figure A.14: Radial displacement after relaxation for the plating-web fillet weld with varied outward bending stress. Units are shown in mm and the deformation is scaled 25 times.

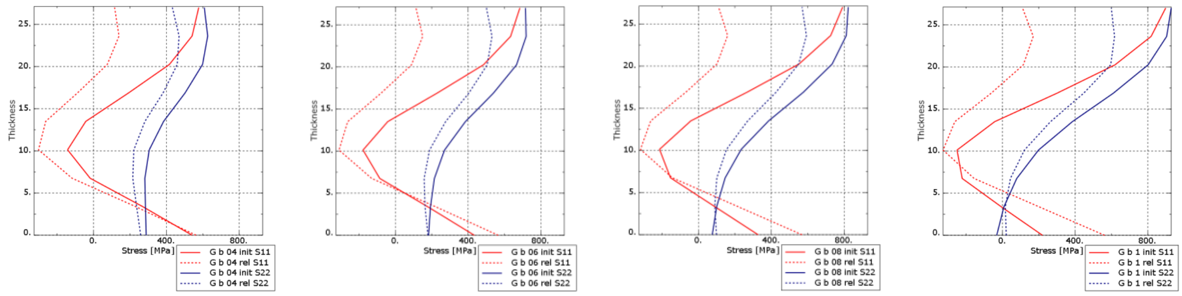

a) $x = 0.4$ b) $x = 0.6$ c) $x = 0.8$ d) $x = 1.0$

Figure A.15: Through-thickness residual stress profiles for the varied inward bending stress in the girth weld. The vertical axis shows the thickness of the material, where 0 corresponds to the inside surface of the plating. The horizontal axis shows stress. The initial stress is shown as a solid line and the relaxed profile as a dashed line. Red indicates axial stress ($S11$)and blue indicates hoop stress ($S22$).

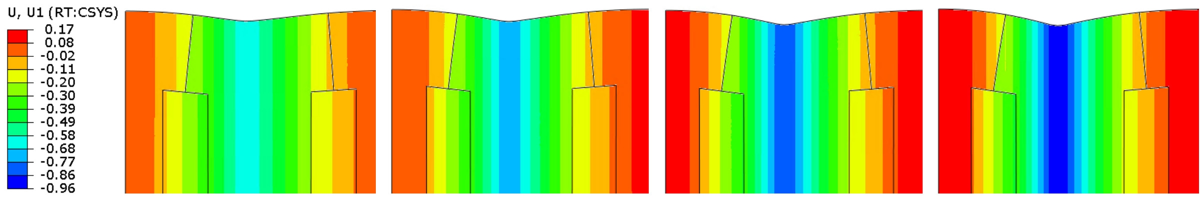

a) $x = 0.4$ b) $x = 0.6$ c) $x = 0.8$ d) $x = 1.0$

Figure A.16: Radial displacement after relaxation for the plating-web fillet weld with varied inward bending stress. Units are shown in mm and the deformation is scaled 25 times.

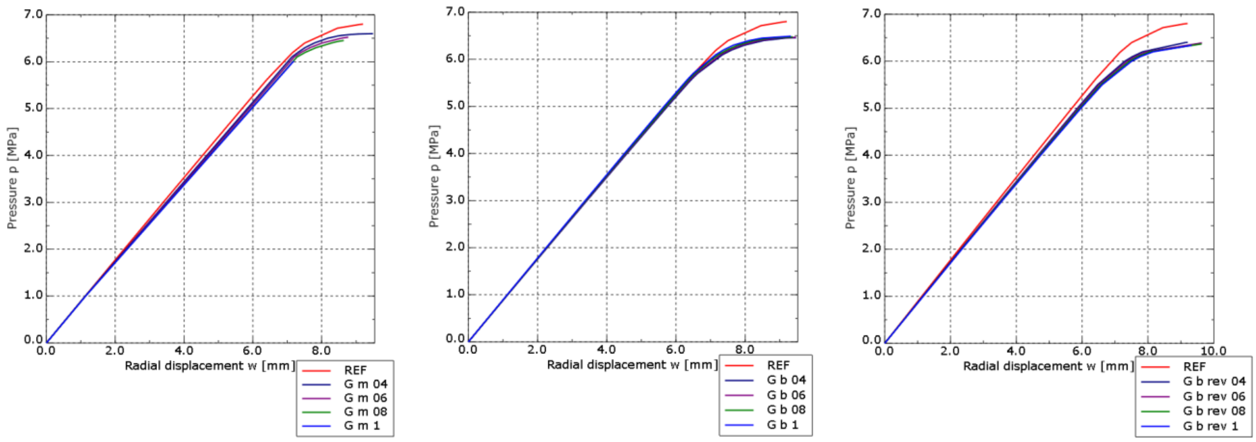

a) pressure-displacement plot for varied membrane stress

b) pressure-displacement plot for different outward bending

c) pressure-displacement plot for different inward bending

Figure A.17: Pressure-displacement response for the girth weld with varied membrane stress and outward and inward bending stress.

A5 - Seam weld

Table A.5 present the results for the seam weld with varied membrane stress bending stress. Varying the membrane stress shows the largest change in w_{max} while both show a similar effect on δw which in this case describes the out of roundness. Both show small effect on the axial shrinkage δv. Varying both stress components show a nearly constant decrease in collapse pressure over the investigated range, and the pressure displacement curves in Figure A.22 show close to identical response to the ideal reference up until just before the collapse. Detailed through-thickness, and contour plots are shown in Figure A.18 - Figure A.21.

Table A.5: Results for the seam weld with varied membrane and bending stress, including collapse pressure, change in collapse pressure relative to the ideal, stress-free reference analysis, maximum radial displacement after relaxation w_{max}, and measured bay deformations $\delta_w$and δ_v.

Varied parameter	**Multiplier *x***	**Ref**	**0.4**	**0.6**	**0.8**	**1.0**
Membrane	Collapse pressure p_c [MPa]	6.80	6.66	6.68	6.67	6.66
	Change from reference (%)	0.0	-2.1	-1.8	-2.0	-2.0
	w_{max} [mm]	0.0	0.12	0.16	0.21	0.25
	δw [mm]	0.0	0.15	0.21	0.27	0.38
	δv [mm]	0.0	0.0082	0.013	0.017	0.021
Bending	Collapse pressure p_c [MPa]	6.80	6.65	6.67	6.66	6.66
	Change from reference (%)	0.0	-2.1	-2.0	-2.0	-2.0
	w_{max} [mm]	0.0	0.092	0.10	0.11	0.11
	δw [mm]	0.0	0.12	0.11	0.24	0.32
	δv [mm]	0.0	0.019	0.019	0.018	0.017

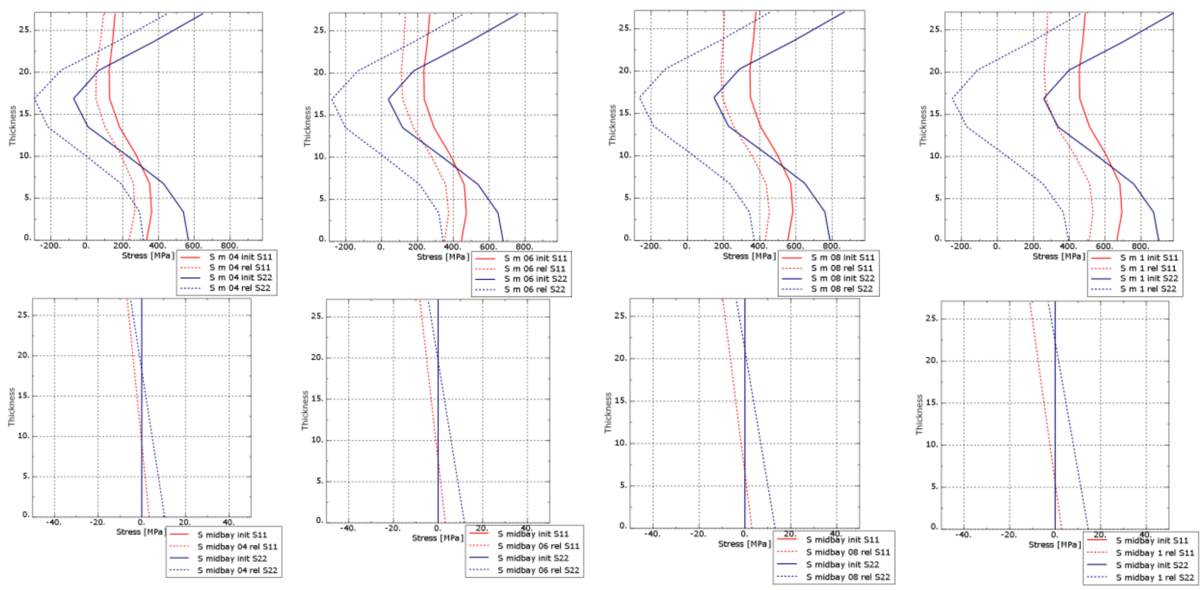

a) $x = 0.4$ b) $x = 0.6$ c) $x = 0.8$ d) $x = 1.0$

Figure A.18: Through-thickness residual stress profiles for the varied membrane stress in the seam weld and the corresponding midbay response. The vertical axis shows the thickness of the material, where 0 corresponds to the inside surface of the plating. The horizontal axis shows stress. The initial stress is shown as a solid line and the relaxed profile as a dashed line. Red indicates axial stress ($S11$)and blue indicates hoop stress ($S22$).

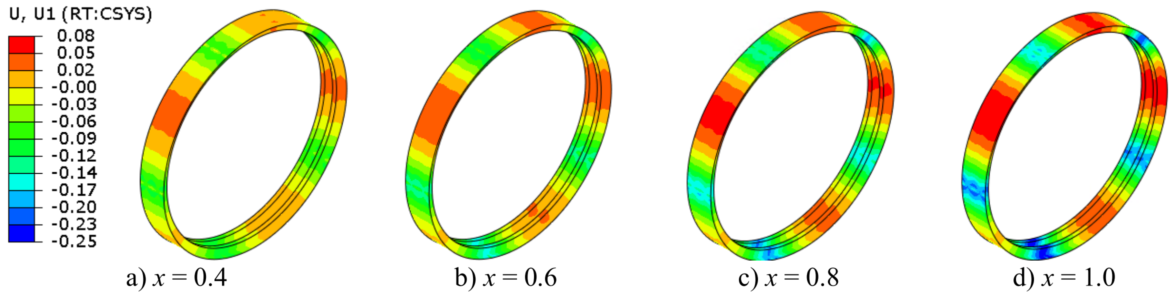

Figure A.19: Radial displacement after relaxation for the seam weld with varied membrane stress. Units are shown in mm and the deformation is scaled 25 times.

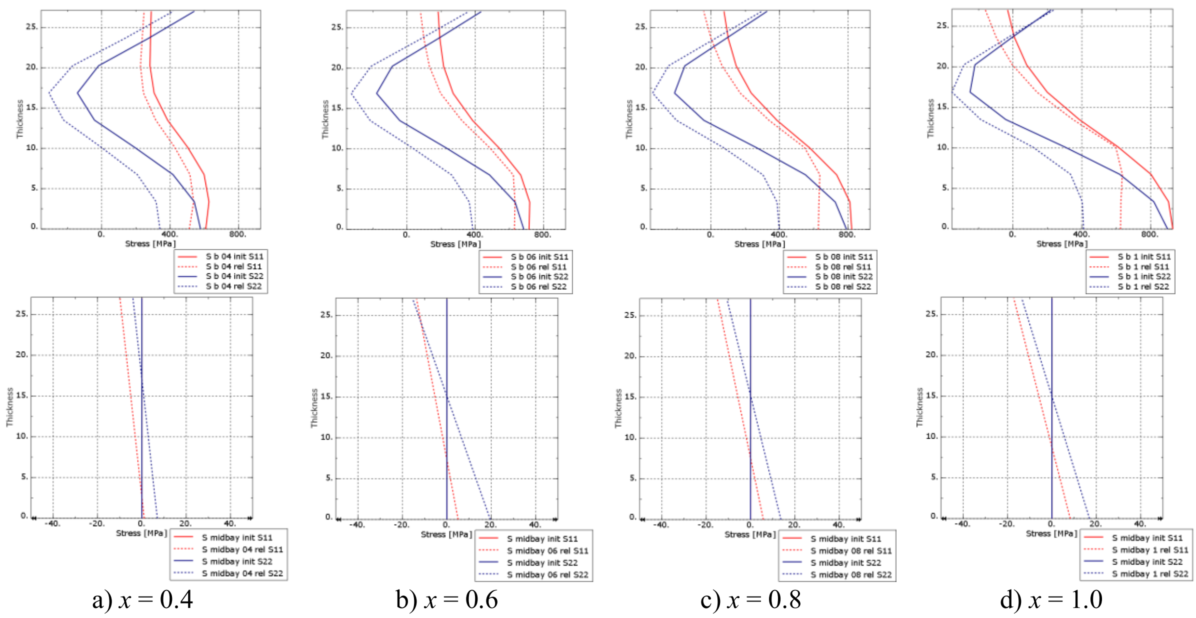

Figure A.20: Through-thickness residual stress profiles for the varied bending stress in the seam weld and the corresponding midbay response. The vertical axis shows the thickness of the material, where 0 corresponds to the inside surface of the plating. The horizontal axis shows stress. The initial stress is shown as a solid line and the relaxed profile as a dashed line. Red indicates axial stress ($S11$)and blue indicates hoop stress ($S22$).

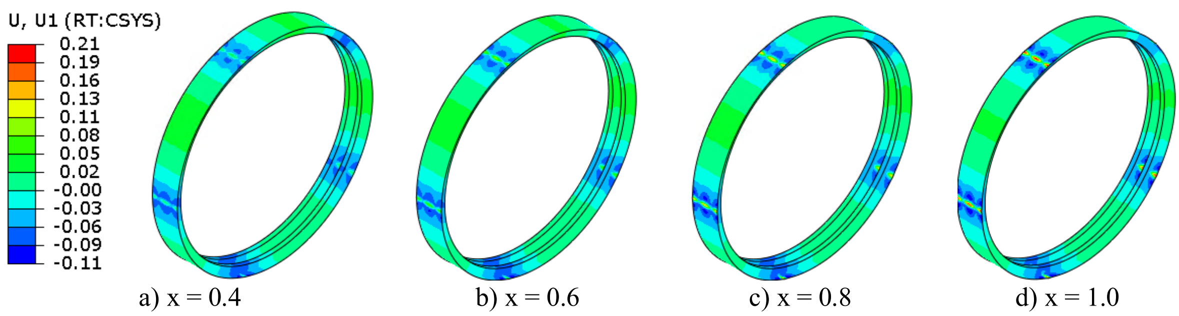

Figure A.21: Radial displacement after relaxation for the seam weld with varied bending stress. Units are shown in mm and the deformation is scaled 25 times.

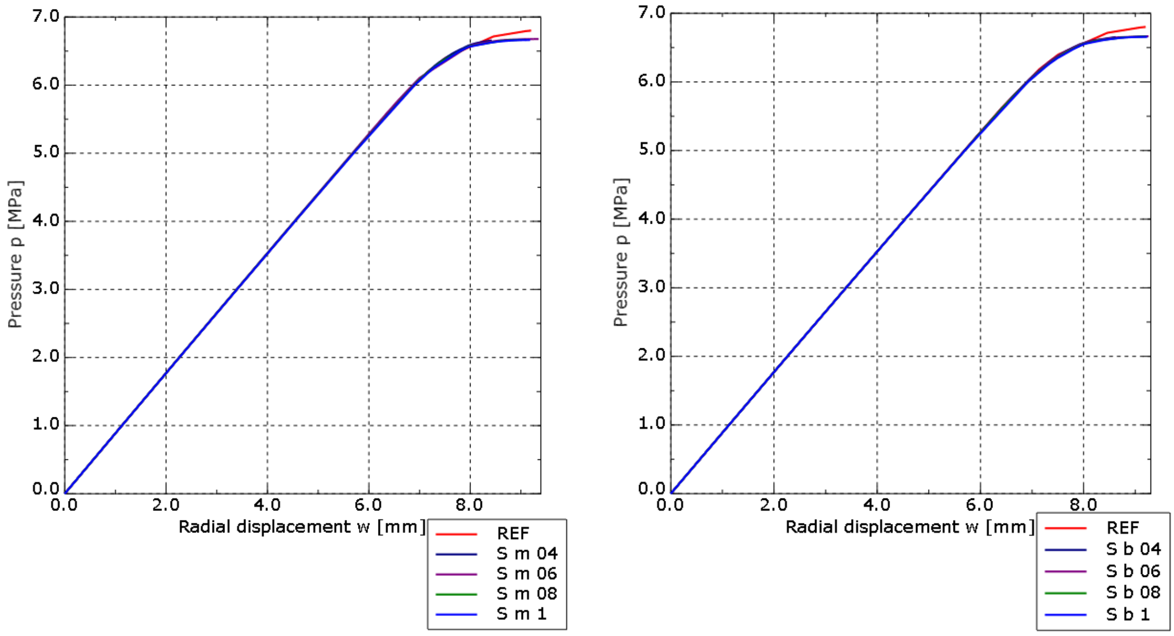

a) pressure-displacement plot for varied membrane stress

b) pressure-displacement plot for varied bending stress

Figure A.22: Pressure-displacement response for the seam weld with varied membrane and bending stress.